

Study of Chemically Peculiar Stars-I : High-resolution Spectroscopy and K2 Photometry of Am Stars in the Region of M44

Santosh Joshi¹★, Otto Trust²†, E. Semenko^{3,4}, P. E. Williams⁵, P. Lampens⁶, P. De Cat⁶, L. Vermeylen⁶, D. L. Holdsworth⁷, R. A. García^{8,9}, S. Mathur^{10,11}, A. R. G. Santos^{12,13}, D. Mkrtichian³, A. Goswami¹⁴, M. Cuntz¹⁵, A. P. Yadav¹⁶, M. Sarkar¹, B. C. Bhatt¹⁴, F. Kahraman Aliçavuş^{17,18}, M. D. Nhlapo¹⁹, M. N. Lund²⁰, P. P. Goswami¹⁴, I. Savanov²¹, A. Jorissen²², E. Jurua², E. Avvakumova²³, E. S. Dmitrienko²⁴, N. K. Chakradhari²⁵, M. K. Das²⁶, S. Chowdhury¹⁷, O. P. Abedigamba^{19,27}, I. Yakunin⁴, B. Letarte¹⁹, and D. Karinkuzhi²⁸

Affiliations are listed at the end of the paper

Accepted XXX. Received YYY; in original form ZZZ

ABSTRACT

We present a study based on the high-resolution spectroscopy and *K2* space photometry of five chemically peculiar stars in the region of the open cluster M44. The analysis of the high-precision photometric *K2* data reveals that the light variations in HD 73045 and HD 76310 are rotational in nature and caused by spots or cloud-like co-rotating structures, which are non-stationary and short-lived. The time-resolved radial velocity measurements, in combination with the *K2* photometry, confirm that HD 73045 does not show any periodic variability on timescales shorter than 1.3 d, contrary to previous reports in the literature. In addition to these new rotational variables, we discovered a new heartbeat system, HD 73619, where no pulsational signatures are seen. The spectroscopic and spectropolarimetric analyses indicate that HD 73619 belongs to the peculiar Am class, with either a weak or no magnetic field considering the 200 G detection limit of our study. The Least-Squares Deconvolution (LSD) profiles for HD 76310 indicate a complex structure in its spectra suggesting that this star is either part of a binary system or surrounded by a cloud shell. When placed in the Hertzsprung-Russell diagram, all studied stars are evolved from main-sequence and situated in the δ Scuti instability strip. The present work is relevant for further detailed studies of CP stars, such as inhomogeneities (including spots) in the absence of magnetic fields and the origin of the pulsational variability in heartbeat systems.

Key words: Stars: chemically peculiar – stars: individual (HD 73045, HD 73574, HD 73618, HD 73619, HD 76310) – stars: rotation, techniques – photometry, spectroscopy, spectropolarimetry

1 INTRODUCTION

The chemically peculiar (CP) stars are a group of main sequence (MS) B-, A-, and F-type stars having peculiar surface elemental abundances; they are characterized by abnormal spectral lines strengths (Preston 1974). The chemical anomalies in these stars are thought to be confined to the outer stellar layers and to arise from gravitational settling and radiative levitation of certain elements, a process known as atomic diffusion (Michaud 1970; Michaud et al. 1981). The present study is confined to one subset of CP stars, the metallic-lined A (Am) stars, which are generally non-magnetic in nature and characterized by under-abundances of some light elements such as Ca and Sc, but slight/moderate over-abundances of iron peak elements, e.g., Zn, Sr, Y, Zr, and Ba. The projected rotational velocities of these stars are generally smaller than for ordinary A stars ($v \sin i$ typically $< 120 \text{ km s}^{-1}$), with the majority of the Am stars being members of

close binary systems. Rotational braking through tidal interaction is regarded as a possible cause of the low rotational velocities.

Using four years of high-precision photometry from the nominal *Kepler* mission and the *K2* campaigns, Balona et al. (2015) investigated the light variations in 29 Am stars and found that most of the Am stars in the *Kepler* field have light curves with the characteristics of rotational modulation arising from star spots or co-rotating structures. The origin of spots in Am stars seems to be different from solar-like spots as these stars do not show any signs of intense magnetic fields able to produce such magnetic features. Magnetic fields on the order of sub-Gauss strengths have been reported in some Am stars, e.g., Sirius A (Petit et al. 2011), Vega (Böhm et al. 2015), β UMa, and θ Leo (Blazère et al. 2015), Alhena (Blazère et al. 2016) and ρ Pup (Neiner et al. 2017). It is thought that for the majority of these stars that convective flows in the atmospheres may disrupt any spot-like features (Kupka 2003). Hence, the rotational modulation in some Am stars indicates that either a weak magnetic field may lead to surface inhomogeneities in the form of spots across the stellar surface or, alternatively, there is some unknown mechanism(s) producing those spots. If a weak magnetic field is indeed present, then

★ E-mail: santosh@aries.res.in

† E-mail: otrust@must.ac.ug

the basic processes operating in Am stars would need to be revisited since magnetic fields have been omitted from the diffusion models attempting to explain their unusual chemical abundances (Guzik 2021).

Stars showing variable amplitudes or harmonics in their light curves provide the best cases for identifying rotational modulation. However, it is extremely difficult to distinguish between rotation and binarity at low frequencies, noting that the amplitude of the periodic variation due to co-rotating star spots changes in a relatively short time-scale (perhaps a few months).

Short-term variability, similar to that seen in δ Scuti stars, has been reported in many Am stars and is understood to arise from pulsations driven by the κ -mechanism operating in the He II ionization zone (Pamyatnykh 2000) combined with turbulent pressure in the H/He I ionization zone (Smalley et al. 2017; Antoci et al. 2019). In the context of the present study, Joshi et al. (2015) suspected a short-term pulsational variability in HD 73045; hitherto awaiting confirmation.

In close binary systems, stellar pulsations may also be tidally induced (Kumar et al. 1995; Thompson et al. 2012); e.g., KOI-54 (Welsh et al. 2011; Fuller & Lai 2012; Burkart et al. 2012; O’Leary & Burkart 2014) and KIC 3230227 (Guo et al. 2017). Highly eccentric ($e > 0.3$) binary systems with orbital periods between a fraction of a day and tens of days showing a sudden increase in brightness at periastron passage, on the order of several parts-per-thousand (ppt), are known as heartbeat (HB) stars (Handler et al. 2002; Maceroni et al. 2009; Hambleton et al. 2013; Beck et al. 2014; Hambleton et al. 2016, 2018; Kołaczek-Szymański et al. 2020). The name stems from the resemblance of the light curve to a heartbeat in an electrocardiogram. About 180 heartbeat stars have been discovered to date. Due to the small-amplitude light variations and their short orbital periods, these targets were mainly detected using space missions such as *Kepler* (Hambleton et al. 2013; Kirk et al. 2016; Hambleton et al. 2016; Fuller 2017; Hambleton et al. 2018; Guo et al. 2020). The Am stars are often part of binary systems (Carquillat & Prieur 2007), though Am stars in heartbeat systems have not been reported in the literature yet, thus the discovery of a new heartbeat beat system in one of the CP stars HD 73619 would be significant.

In the present work, we revisit all stars previously observed as part of the Nainital-Cape survey project (Ashoka et al. 2000; Martinez et al. 2001; Joshi et al. 2003, 2006, 2009, 2010, 2012, 2016, 2017) with data in the *Kepler* and *K2* archives. It is our aim to search for low frequency, high-precision, and photometric variability. No stars from the Nainital-Cape survey were observed in the nominal *Kepler* field, whilst eight stars were found in the *K2* archive. In the current paper, we present the results on extrinsic (rotational and heartbeat) variables, as well as the results for stars where variability could not be ascertained.

2 OBSERVATIONS AND DATA REDUCTION

The photometric observations were obtained using both ground- and space-based telescopes while spectroscopy and spectropolarimetry were performed through ground-based telescopes. The specifications of the telescopes and state-of-art instruments used for the observations are listed in Table 1.

2.1 Ground-Based Differential Photometry of HD 73045

To investigate the variability of the single-lined spectroscopic binary (SB1) HD 73045, as suspected by Joshi et al. (2015), this object was extensively monitored photometrically with the 1.3-m Dev-

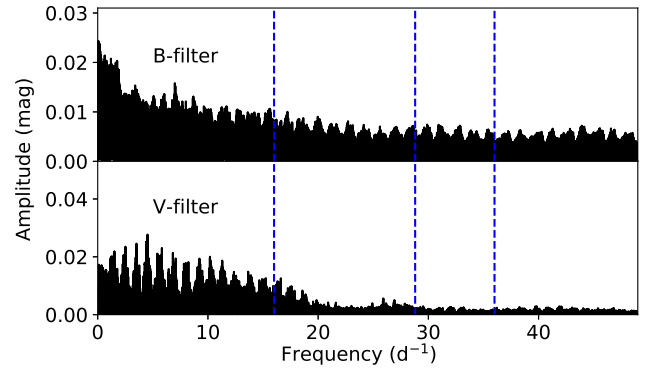


Figure 1. The amplitude spectra of HD 73045 using the combined data from ground-based observations in B (top panel) and V (bottom panel) filters. There are no significant frequencies with signal-to-noise ratio (SNR) above 4 (0.048 mag for B-filter and 0.051 mag for V-filter), hence the star is classified as non-variable. The blue dashed vertical lines represent the short-term periodicity as suspected by Joshi et al. (2015).

asthal Fast Optical Telescope (DFOT; Sagar et al. 2011), the 1.04-m Sampurnanand Telescope (ST; Sinval et al. 1972), the 2×0.40-m MASTER-II-URAL telescope (Lipunov et al. 2010), and the 0.6-m Panchromatic Robotic Optical Monitoring and Polarimetry Telescope (PROMPT-8; Burdanov et al. 2014). These instruments are introduced in Table 1.

All observations were carried out through a Johnson B and/or V filter. Calibration frames were acquired during each night for the correction of background and pixel sensitivity. The science frames were processed by subtracting master bias and dark frames before normalising them with a median flat-field frame from which the cosmic rays were removed. The instrumental magnitudes of HD 73045 and the comparison stars (BD +19°2046 and TYC 1395-855-1) were obtained through aperture photometry using the in-built *DAOPHOT* package of IRAF (Davis 1994). The characteristics of the ground based photometric observations are given in Table C1 and the individual light curves and power spectra are presented in Figs. C1 and C2. The top and bottom panels of Fig. 1 show the combined amplitude spectra of HD 73045 in the B and V filters, respectively.

2.2 K2 Space Photometry

Our target stars were observed by the *K2* mission that operated in a long cadence (LC; 29.4 min) and a short cadence (SC; 58.8 s) mode (Howell et al. 2014). *K2* pointed towards the Praesepe (Beehive) cluster (M44) during the campaigns C05 (2015/04/27–2015/07/10), C16 (2017/12/07–2018/02/25), and C18 (2018/05/12–2018/07/02). The *K2* observations of our targets are summarized in Table 2.

These photometric data sets were downloaded from the Barbara A. Mikulski Archive for Space Telescopes (MAST) database¹. Each target pixel file (TPF) was checked for the presence of additional stars. As HD 73045, HD 76310, and HD 73574 were the sole stars in their TPF images, their respective *K2* FITS light curve files were directly downloaded in the PDC_SAP format (Stumpe et al. 2012; Smith et al. 2012), having undergone pre-search data conditioning (PDC) processing of their simple aperture photometry (SAP) flux data. The underlying position-dependent artifacts were removed by

¹ <https://archive.stsci.edu/k2/epic/search.php>

Table 1. The specifications of the telescopes and back-end instruments used for the photometric and spectroscopic observations.

Category	Name of Telescope	Diameter (m)	Location	Detector/Spectrograph	FoV/Resolution
Ground-based Photometry	DFOT	1.30	Devasthal (India)	Andor's DZ436	$18' \times 18'$
				Andor's iXon EM+ DU-897	$4.7' \times 4.7'$
	ST	1.04	Nainital (India)	2k Wright CCD	$13' \times 13'$
	MASTER-II-URAL	0.40	Ural Federal University (Russia)	U16M CCD	$2^\circ \times 4^\circ$
	PROMPT-8	0.60	CTIO (Chile)	Apogee, F42	$26.6' \times 22.6'$
Space-based Photometry	K2	0.95	Space	e2v CCD90s	$10.25^\circ \times 10.25^\circ$
Spectroscopy	BTA	6.00	Nizhniy Arkhyz (Russia)	NES,MSS	39 000, 15 000
	TNO	2.40	Chiang Mai (Thailand)	MRES	17 000
	HCT	2.00	Hanle (India)	HESP	30 000
	Mercator	1.20	La Palma (Spain)	HERMES	85 000

Table 2. The K2 campaigns concerning our programme stars.

Star Name	EPIC Number	K2 Observation Campaigns					
		C05 ~79 d		C16 ~80 d		C18 ~50 d	
		LC	SC	LC	SC	LC	SC
HD 73045	211910450	✓	-	-	-	✓	✓
HD 73574	211989558	✓	-	-	-	✓	-
HD 73618	211955190	✓	-	✓	-	✓	-
HD 73619	211954496	✓	-	✓	-	✓	-
HD 76310	212082764	✓	-	✓	-	✓	-

processing the data through the K2SC algorithm (Aigrain et al. 2015). The TPF images of HD 73618 and HD 73619 showed the presence of nearby stars (Fig. 2), which had to be masked out to isolate the flux of these target stars. The remaining images were averaged and a custom mask was produced to isolate the target star. This mask was applied to each image of the campaign and the total flux for each image was deduced, producing a light curve similar to the available SAP flux data. These data sets were further processed with the K2SC algorithm. Fig. 3 (top-left, in blue) shows an example light curve for the C18 observation of HD 73045. A detailed discussion of our analysis is given in Appendix B. A periodogram produced by the Lomb-Scargle algorithm is shown in Fig. 3 (bottom, in blue). The frequency-varying artifact in the light-curve is due to the roll-angle variation (Aigrain et al. 2016), reversing twice near 10 and 40 days respectively. This artifact is not prevalent in the periodogram, but is distributed between 0.25–2 days ($0.5-4 \text{ d}^{-1}$).

Using a multi-component sinusoidal model, frequencies, periods, amplitudes, and phases, relating to the variability detected in the K2 light curves, are derived, and are tabulated in Table 3. Fig. 3 (top-left, in red) illustrates such a model of the HD 73045 C18 light curve, for which the derived amplitudes and frequencies of the components are included in the periodogram (Fig. 3, bottom) as red stems. The light curve data is phase-folded on the period with the largest amplitude and overplotted with that period's sinusoidal component (Fig. 3, top-

right). Similar figures for the remaining campaigns of all targets are given in Appendix C (Figs. C7–C18).

2.3 High-Resolution Spectroscopic and Spectropolarimetric Observations

High-resolution spectroscopy provides an opportunity of deriving a wide range of information on the target stars, such as basic stellar parameters like the effective temperature (T_{eff}), surface gravity ($\log g$), and metallicity ($[M/H]$). The high-resolution spectra of our targets were gathered with four spectrographs: (1) the Hanle Échelle Spectrograph (HESP; Chanumolu et al. 2015; Sriram et al. 2018) at the 2.01-m Himalayan Chandra Telescope (HCT) of IIA, Bengaluru, (2) the Middle Resolution Échelle Spectrograph (MRES) at the 2.4-m telescope of the TNO (Thailand), (3) the High Efficiency and Resolution Mercator Échelle Spectrograph (HERMES; Raskin et al. 2011) at the 1.2-m Mercator telescope, and (4) the Nasmyth Échelle Spectrometer (NES; Panchuk et al. 2017) at the 6-m Bolshoi Teleskop Alt-azimutalnyi (BTA) of the Special Astrophysical Observatory (SAO; Russia).

For HD 73619, we also used the Main Stellar Spectrograph (MSS; Chountonov 2004; Panchuk et al. 2014) at the 6-m BTA for measuring stellar magnetic field strengths. Our target was observed along with two standard stars, i.e., HD 52711 (non-magnetic) and 53 Cam (magnetic). These spectropolarimetric observations were carried out in a series of paired exposures obtained in two orthogonal orientations of a retarder.

Data reduction was performed using the pipeline developed for each particular spectrograph that generally involves overscan correction, averaged bias subtraction, flat-field correction, and wavelength calibration. The spectropolarimetric data reduction was performed using the ZEEMAN package developed within the ESO MIDAS environment for the specific format of CCD spectra taken with an image slicer (Kudryavtsev et al. 2006).

Table 3. Parameters of the sinusoidal component (ordered by amplitude), related to the variations observed within the analysed flux data, as derived from the fitting process. For each data set, these components have been summed to produce a model of their respective light curves.

Star Name	Campaign	Frequency (d ⁻¹)	Period (d)	Amplitude (mmag)	Phase (rad)
HD 73045	C05	0.0783 ± 0.0002	12.77 ± 0.03	0.113 ± 0.003	1.44 ± 0.03
		0.1555 ± 0.0005	6.43 ± 0.02	0.035 ± 0.002	-0.47 ± 0.06
		0.0640 ± 0.0005	15.6 ± 0.1	0.030 ± 0.002	-2.38 ± 0.07
		0.1395 ± 0.0006	7.17 ± 0.03	0.026 ± 0.002	-1.31 ± 0.08
		0.1668 ± 0.0008	6.00 ± 0.03	0.020 ± 0.002	-0.9 ± 0.1
	C18	0.0791 ± 0.0005	12.64 ± 0.08	0.039 ± 0.002	-0.008 ± 0.05
		0.1535 ± 0.0008	6.51 ± 0.03	0.023 ± 0.002	-0.54 ± 0.07
HD 76310	C05	0.2165 ± 0.0002	4.618 ± 0.004	0.50 ± 0.01	2.81 ± 0.02
		0.2039 ± 0.0002	4.905 ± 0.005	0.320 ± 0.008	-1.39 ± 0.03
		0.2290 ± 0.0002	4.367 ± 0.005	0.197 ± 0.007	0.19 ± 0.03
		0.1863 ± 0.0003	5.366 ± 0.008	0.149 ± 0.006	-0.84 ± 0.04
		0.4198 ± 0.0004	2.382 ± 0.002	0.106 ± 0.005	-2.56 ± 0.05
		0.1668 ± 0.0004	5.99 ± 0.01	0.099 ± 0.004	-2.75 ± 0.05
	C16	0.2089 ± 0.0002	4.786 ± 0.004	0.40 ± 0.01	-2.22 ± 0.02
		0.1856 ± 0.0002	5.388 ± 0.005	0.315 ± 0.008	-0.65 ± 0.02
		0.0756 ± 0.0004	13.23 ± 0.07	0.099 ± 0.006	0.90 ± 0.06
		0.4302 ± 0.0004	2.325 ± 0.002	0.084 ± 0.005	-2.51 ± 0.06
		0.9699 ± 0.0004	1.0310 ± 0.0005	0.080 ± 0.005	-2.25 ± 0.06
		0.0573 ± 0.0005	17.4 ± 0.2	0.065 ± 0.005	2.95 ± 0.08
	C18	0.2065 ± 0.0002	4.843 ± 0.006	1.09 ± 0.02	-1.05 ± 0.02
		0.1841 ± 0.0005	5.43 ± 0.02	0.25 ± 0.01	-2.47 ± 0.04
		0.4270 ± 0.0006	2.342 ± 0.003	0.18 ± 0.01	-2.4 ± 0.06
HD 73574	C05	0.0700 ± 0.0004	14.28 ± 0.08	0.85 ± 0.04	2.87 ± 0.05
		0.0925 ± 0.0008	10.8 ± 0.1	0.36 ± 0.04	1.7 ± 0.1
	C18	0.092 ± 0.002	10.8 ± 0.2	0.047 ± 0.007	0.4 ± 0.1
HD 73618	C05	0.2644 ± 0.0002	3.782 ± 0.003	0.40 ± 0.01	1.89 ± 0.03
		0.2055 ± 0.0002	4.867 ± 0.006	0.248 ± 0.008	0.90 ± 0.03
		0.4100 ± 0.0004	2.439 ± 0.002	0.136 ± 0.007	2.98 ± 0.05
		0.2531 ± 0.0005	3.951 ± 0.008	0.094 ± 0.006	2.78 ± 0.07
		0.4287 ± 0.0005	2.333 ± 0.003	0.092 ± 0.006	1.00 ± 0.07
		0.1766 ± 0.0006	5.66 ± 0.02	0.077 ± 0.006	-1.81 ± 0.08
	C16	0.2609 ± 0.0002	3.833 ± 0.003	0.32 ± 0.009	1.28 ± 0.03
		0.2052 ± 0.0002	4.874 ± 0.004	0.268 ± 0.007	2.74 ± 0.03
		0.4013 ± 0.0003	2.493 ± 0.002	0.151 ± 0.005	-2.03 ± 0.04
		0.2244 ± 0.0003	4.456 ± 0.005	0.125 ± 0.005	2.86 ± 0.04
		0.4167 ± 0.0003	2.399 ± 0.002	0.099 ± 0.004	2.51 ± 0.05
		0.2365 ± 0.0003	4.228 ± 0.006	0.085 ± 0.004	-2.90 ± 0.05
		0.2877 ± 0.0004	3.476 ± 0.005	0.066 ± 0.004	-0.23 ± 0.06
		0.4471 ± 0.0005	2.237 ± 0.002	0.062 ± 0.004	1.49 ± 0.06
	C18	0.2656 ± 0.0003	3.765 ± 0.004	0.60 ± 0.01	-1.54 ± 0.02
		0.2120 ± 0.0004	4.717 ± 0.009	0.224 ± 0.008	1.47 ± 0.04
		0.1951 ± 0.0005	5.13 ± 0.01	0.174 ± 0.007	-0.80 ± 0.04
		0.4180 ± 0.0004	2.392 ± 0.002	0.173 ± 0.007	2.89 ± 0.04
		0.2373 ± 0.0005	4.22 ± 0.01	0.113 ± 0.006	2.11 ± 0.05
		0.2941 ± 0.0005	3.401 ± 0.006	0.111 ± 0.005	-0.38 ± 0.05
HD 73619	C05	0.0771 ± 0.0002	12.97 ± 0.03	0.394 ± 0.009	-2.01 ± 0.02
		0.1548 ± 0.0002	6.46 ± 0.01	0.208 ± 0.007	-2.91 ± 0.03
		0.2326 ± 0.0003	4.300 ± 0.005	0.144 ± 0.006	2.52 ± 0.04
		0.3104 ± 0.0005	3.221 ± 0.005	0.085 ± 0.005	1.45 ± 0.06
		0.3882 ± 0.0006	2.576 ± 0.004	0.059 ± 0.005	0.77 ± 0.09
		0.465 ± 0.001	2.152 ± 0.005	0.033 ± 0.005	0.3 ± 0.1
		0.545 ± 0.001	1.834 ± 0.005	0.025 ± 0.005	-2.1 ± 0.2
	C18	0.0775 ± 0.0003	12.92 ± 0.05	0.344 ± 0.01	-1.27 ± 0.03
		0.1525 ± 0.0004	6.46 ± 0.02	0.179 ± 0.007	-0.9 ± 0.04
		0.2294 ± 0.0006	4.36 ± 0.01	0.113 ± 0.006	-0.81 ± 0.05
		0.3063 ± 0.006	3.265 ± 0.008	0.074 ± 0.005	-0.77 ± 0.07
		0.384 ± 0.001	2.607 ± 0.007	0.049 ± 0.005	-0.6 ± 0.1
		0.462 ± 0.002	2.16 ± 0.01	0.023 ± 0.005	-0.5 ± 0.2
		0.540 ± 0.003	1.85 ± 0.01	0.017 ± 0.005	-0.2 ± 0.3

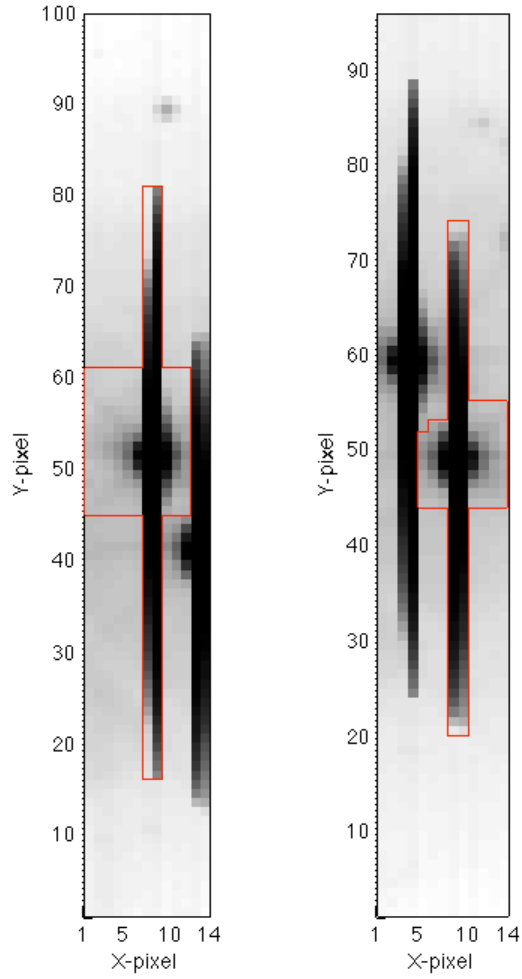


Figure 2. Target pixel images from the C18 time-series of HD 73618 (left) and HD 73619 (right). Note that each star appears in both images. The red border signifies the boundary of a custom mask within which the pixels are isolated and summed to produce a single simple aperture photometry flux data point.

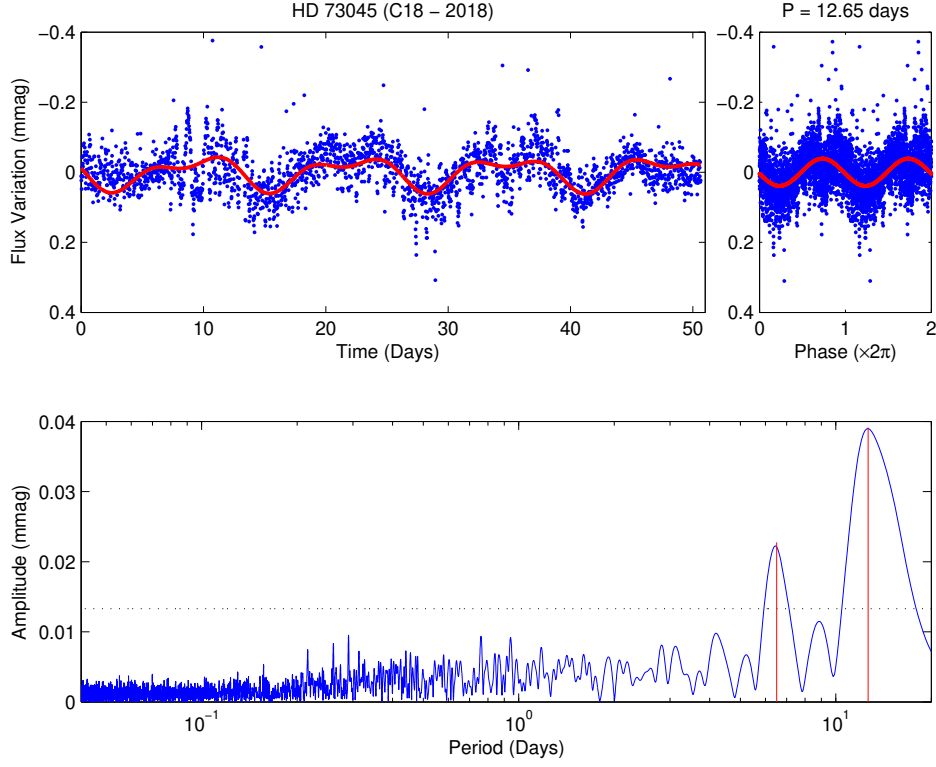


Figure 3. Top left: Time-series illustrating photometric flux variation (in mmag) of HD 73045 for the LC 2018 *K2* Campaign 18. The data (blue points) include intrinsic signals as well as systemic and noise artifacts. The sinusoidal model, with parameters given in Table 3, is shown as the red line. Top right: The photometric data (blue points) phase folded on the dominant variation period of 12.2 d. The red line represents the best-fit to this data. The data is repeated over two periods for clarity of presentation. Bottom: Linear-log periodogram of spectral amplitudes (blue line), in mmag. The components of the sinusoidal model are shown by the red stems. The black dotted line corresponds to a False Alarm Probability of 10^{-8} , and the periodogram peaks above this line are considered to be confirmed signals.

3 RADIAL VELOCITY MEASUREMENTS

We measured the radial velocities (RVs) of all target stars using the Least-Squares Deconvolution (LSD) technique (Kochukhov et al. 2010). For HD 73045, the obtained RV time-series data were analysed using the standard Discrete Fourier Transform (DFT) technique. The results of the RV analysis for HD 73045 obtained from HERMES and MRES are shown in Figs. C3 and C4, respectively. The frequency spectra at different epochs do not show any significant peak with $\text{SNR} > 4$. Therefore, we conclude that in the observational limit ($3\sigma \sim 300 \text{ m s}^{-1}$), HD 73045 does not vary spectroscopically on a short time scale. The RV of HD 73045 was also measured from the single spectrum from NES. All RV measurements are plotted with the orbital parameters given by Carquillat & Prieur (2007), see Fig. C5. Based on the residuals shown in the bottom panel of Fig. C5, our results are consistent with the known orbital solution (with an orbital period of 435.57 days).

For HD 73619, the RV measurements based on the MSS and HESP spectra (see Table 5) are fitted well using the orbital parameters (with an orbital period of 12.91 days) derived by Debernardi et al. (2000). Fig. 4 shows the orbital solution of HD 73619 where the observations are compared to the model. Our RV observations for both HD 73045 and HD 73619 agree with the known orbital parameters; hence, we did not re-derive them.

Table 4. Summary of the high-resolution spectroscopic observations. Spectropolarimetric observations are listed in the last row (MSS BTA).

Spectrograph Telescope				
Star	HJD (2 450 000+) (day)	Total No. Spectra	Spectral Range (nm)	SNR
MRES @ TNT				
HD 73045	7007.391 – 7007.467	38	406 – 879	33 – 310
	7009.408 – 7009.470	29		(@ 572 nm)
	7011.365 – 7011.470	31		
HD 76310	8954.116	1		
NES @ BTA				
HD 73045	7350.462	1	409 – 686	300 (@ 555 nm)
HERME @ Mercator				
HD 73045	7490.375 – 7490.496	30	390 – 893	40 – 45
	7491.377 – 7491.425	10		(@ 650 nm)
	7512.375 – 7512.460	22		
HESP @ HCT				
HD 73574	8473.186	1	350 – 1000	143
HD 73619	8473.223	1		96
HD 76310	8473.261	1		100
HD 73618	8555.074	1		220 (@ 550 nm)
MSS @ BTA				
HD 73619	8578.300 – 8578.330	3	444 – 498	150 – 200
	8579.293 – 8579.314	3		100 – 250 (@ 455 nm)

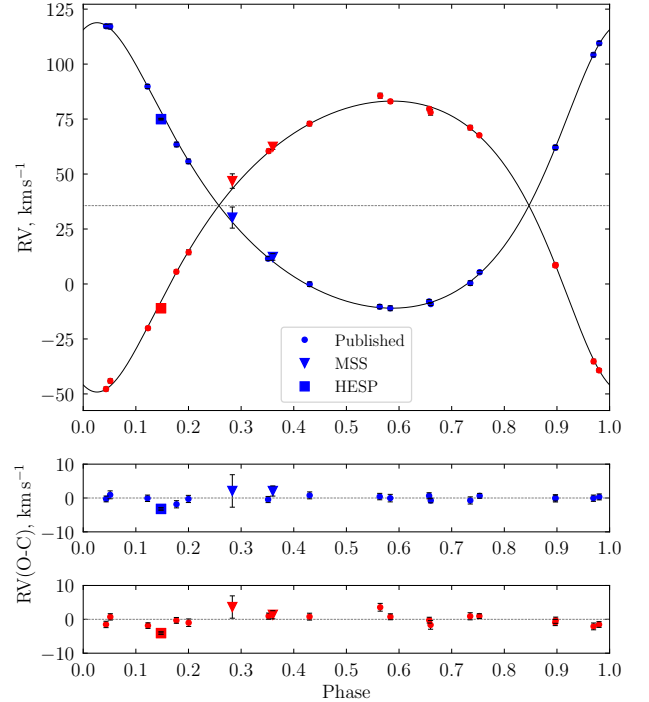


Figure 4. Radial velocity measurements of HD 73619 derived from both the HESP and MSS spectra are plotted together with the orbital solution given by Debernardi et al. (2000). Blue and red symbols represent the measured RV of the primary and secondary component, respectively.

Table 5. Basic parameters of the components of HD 73619 and HD 76310 obtained through high-resolution spectroscopy. The numbers 1 and 2 are assigned to the primary and secondary component, respectively. The spectral coverage was 430–680 nm. We assumed equal light factors for both components of HD 73619, whereas for HD 76310, a light ratio (I_1) of 0.887 was used. The stars HD 73045, HD 73574, and HD 73618 are assumed to be single stars, as either they are truly single, or the secondary star does not contribute significantly to the lines of the spectrum.

Star	Spectrograph	RV (km s ⁻¹)		T_{eff} (K)		log g (cgs)		$v \sin i$ (km s ⁻¹)	
		1	2	1	2	1	2	1	2
HD 73619	HESP	-8.6 ± 0.1	77.5 ± 0.1	7150 ± 90	7220 ± 100	3.28 ± 0.60	3.02 ± 0.12	14.5 ± 0.5	13.3 ± 0.8
	MSS	30.2 ± 4.8	46.8 ± 3.3	7410 ± 370	7200 ± 280	3.90 ± 0.13	3.54 ± 0.22	17.0 ± 2.0	19.5 ± 0.5
		12.3 ± 1.5	62.4 ± 1.2	7380 ± 390	7080 ± 260	4.0	4.0	16.3 ± 4.0	17.3 ± 3.8
HD 76310	HESP	18.9 ± 2.3	10.1 ± 1.8	7420 ± 210	6220 ± 180	4.0	4.0	96 ± 7	9 ± 1
	MRES	27.4 ± 1.8	19.8 ± 2.8	7030 ± 170	6470 ± 220	4.0	4.0	103 ± 8	20.3 ± 3.4
HD 73045*	ESPaDOnS	27.9	-	7570 ± 200	-	4.05 ± 0.2	-	10 ± 0.5	-
HD 73574	HESP	29.2 ± 2.8	-	7700 ± 160	-	4.12 ± 0.21	-	99 ± 5	-
HD 73618*	ESPaDOnS	15.1	-	8170 ± 200	-	4.00 ± 0.19	-	47 ± 3	-
	HESP	39.2 ± 0.5	-	7960 ± 180	-	3.76 ± 0.19	-	56 ± 3	-

*Fossati et al. (2007)

4 ATMOSPHERIC PARAMETERS

Much of the success of astronomy and astrophysics relies on the accurate knowledge about the basic parameters and structure of stars. Using high-resolution spectroscopic data, HD 73045 has been extensively studied by Fossati et al. (2007, 2008); hence, we refrained from re-deriving its atmospheric parameters. To determine the relevant atmospheric parameters, e.g., T_{eff} , log g , etc., for the remaining targets, we used two approaches, namely, photometric calibrations and high-resolution spectral data. We obtained the fundamental atmospheric parameters from photometry using the Geneva, $uvby\beta$, and 2MASS photometric systems (Cutri et al. 2003), as well as via data obtained from the General Catalogue of Photometric Data² (Mermilliod et al. 1997). The reddening parameters $E(B - V)$ and $E(B2 - V1)$ were obtained using a 3-D dust-map (Green 2018; Green et al. 2019) and ratios of total-to-selective absorption computed by Crawford & Mandwewala (1976), respectively. In Table 6, we compiled the known and derived parameters of the programme stars based on multi-colour photometry.

The fundamental atmospheric parameters determined from photometry were used as initial input to facilitate further analyses. Spectroscopic parameters were derived by comparing observed spectra with synthetic ones computed for the adopted atmospheric parameters by using the χ^2 -minimisation method (see Trust et al. 2021 for more detail). The used the radiative transfer code MOOG (Sneden et al. 2012), together with the line-list version 5 of the Gaia-ESO Survey (GES) (wavelength range of 475–685 nm) (Heiter et al. 2015), the solar abundances by Asplund et al. (2009), and the ATLAS9³ atmospheric models of Castelli & Kurucz (2003) through an integrated software iSpec (Blanco-Cuaresma et al. 2014; Blanco-Cuaresma 2019). The atmospheric parameters estimated from the best fits between the calculated and observed spectra are listed in Table 5. The synthetic spectra based on the values of the atmospheric parameters fit the observed spectra well, as shown in Fig. 5.

For HD 73619, the HESP and MSS spectra clearly show the presence of two components (see Fig. 6 and the LSD profiles of Fig. 7).

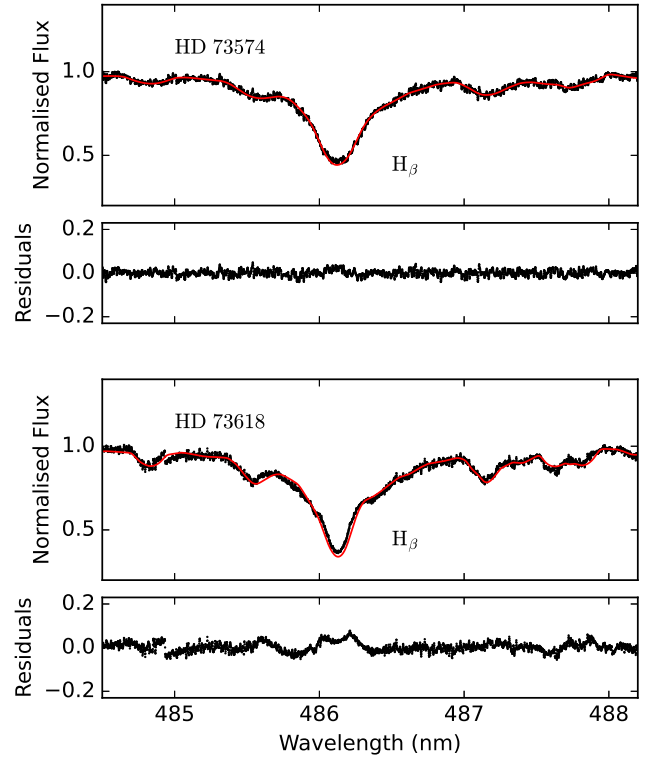


Figure 5. H_β region of the spectra used for the determination of the respective stellar effective temperature. The synthetic spectrum (red) is over-plotted with the observed spectrum (black).

We derived the atmospheric parameters from HESP and MSS spectra using the two-dimensional version of the GIRFIT code developed by Frémat et al. (2006). We reconstructed the composite spectra by searching for the best pair of Doppler shifts and synthetic spectra, one for each component, with solar-like composition in the spectral regions 439–450 nm, 450–470 nm, 470–500 nm, and 510–550 nm.

² <http://obswww.unige.ch/gcpd/indexform.html>

³ http://www.stsci.edu/hst/observatory/crds/castelli_kurucz_atlas.html

Table 6. Basic parameters of the studied stars extracted from various online databases. We list the atmospheric parameters (T_{eff} , $\log g$, and $[M/H]$) computed from the three photometric systems (Geneva, $uvby\beta$ and 2MASS) as well as $\log(L_{\star}/L_{\odot})$ as calculated from the *Gaia* parallaxes.

Star	V^a (mag)	π^b (mas)	$E(B - V)$ (mag)	$E(B2 - V1)$ (mag)	T_{eff} Geneva (± 70 K)	$[M/H]$ Geneva ± 0.08	T_{eff} $uvby\beta$ (± 200 K)	$\log g$ $uvby\beta$ (± 0.10 cgs)	$[M/H]$ $uvby\beta$ ± 0.13	T_{eff} 2MASS (± 190 K)	$\log(L_{\star}/L_{\odot})$	Sp. Type ^c	Peculiarity
HD 73045	8.62	3.7587	0.035	0.0272	7440	0.44	7470	4.28	0.37	7390	1.29 ± 0.10	A7	Am
HD 73574	7.75	5.7064	0.018	0.0138	7870	0.16	7660	3.91	0.15	7730	1.24 ± 0.17	A3	-
HD 73618	7.30	6.9834	0.015	0.0118	7940	0.33	8090	3.90	0.39	7910	1.27 ± 0.13	A0	Am ^{d,e}
HD 73619	7.52	5.4033	0.015	0.0120	7670	0.52	7890	4.17	0.47	7860	1.20 ± 0.06	A0	Am ^f
HD 76310	8.52	5.6101	0.015	0.0117	7310	0.14	7470	4.09	0.25	7320	0.94 ± 0.11	A2	Am ^g

^aHøg et al. (2000), ^bGaia Collaboration (2018), ^cCannon & Pickering (1993), ^dBertaud (1960), ^eRebeiro (1966), ^fBidelman (1956), and ^gCowley & Cowley (1965a)

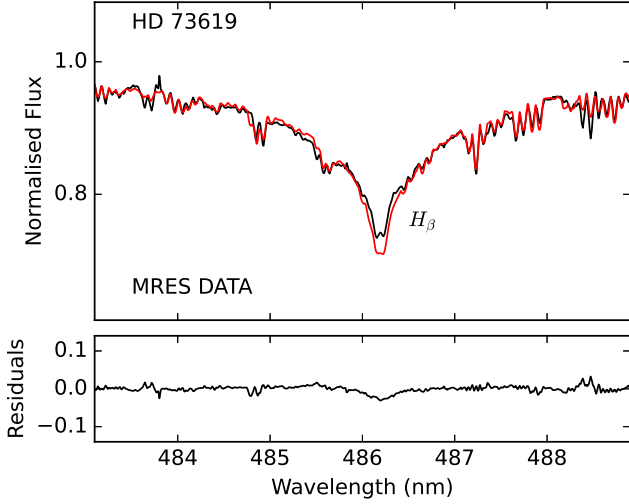


Figure 6. H_{β} section of the MRES spectrum (black) for HD 73619 and the fit (red) using a two-component model and the 2-D version of GIRFIT.

Fig. 6 shows a portion of the HESP spectrum (black) and the fit (red) using a two-component model. The radial velocities as well as the derived atmospheric parameters are listed in Table 5.

5 MAGNETIC FIELD MEASUREMENT OF HD 73619

Magnetic field determinations allow us to distinguish between the two types of CP stars of interest, namely Ap and Am stars. Though spots are thought to occur in the presence of intense magnetic fields, Balona (2013) attributed the photometric variability observed in some A-type stars as due to rotational modulation of stellar surfaces with inhomogeneities in cases where the magnetic field is either weak or absent. The magnetic field can be detected through the Zeeman effect where the left and right circular polarization spectra are shifted with respect to each other with the shift being proportional to the longitudinal magnetic field averaged over the stellar disk (Joshi et al. 2012, and references therein).

We used three techniques to measure the magnetic fields: center of gravity, regression, and LSD. A mean value of 1.23 was adopted for the effective Landé factor that is slightly higher than the corresponding parameter in the original paper by Bagnulo et al. (2002). An example of the intensity and circularly polarized LSD profiles

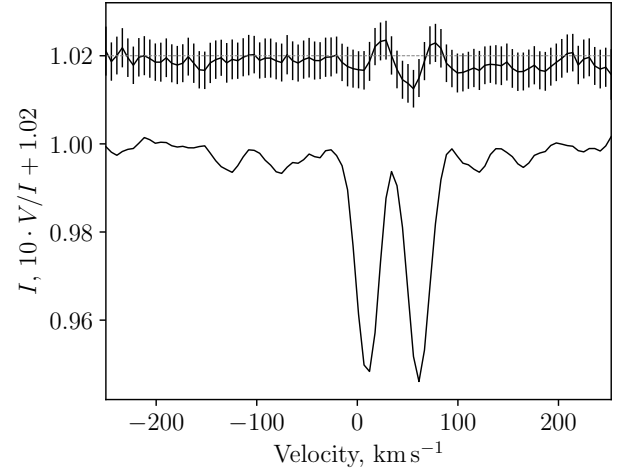


Figure 7. The intensity and circularly polarized LSD profiles of HD 73619.

Table 7. Summary of measurements of longitudinal magnetic field in HD 73619 and the standard stars. The third, fourth, and fifth columns represent the magnetic field measured using classical center of gravity, regression and LSD profiles, respectively. The errors of the magnetic field are given by σ , n is a number of measured lines.

Star Name	HJD (2 450 000+) (day)	$B_z^g \pm \sigma(n)$ (G)	$B_z^r \pm \sigma$ (G)	$B_z^{\text{LSD}} \pm \sigma$ (G)
HD 73619	8578.300	125 ± 50 (215)	120 ± 30	70 ± 50
	8579.293	-150 ± 50 (82) -180 ± 50 (74)	-115 ± 30 -110 ± 25	-30 ± 30
	8578.321	3 ± 50 (267)	10 ± 20	0 ± 40
HD 52711	8579.307	170 ± 50 (244)	150 ± 40	110 ± 30
	53 Cam	8578.330	-4960 ± 150 (204)	-3730 ± 80
53 Cam	8579.314	-3640 ± 150 (204)	-2680 ± 90	-2170 ± 50

of HD 73619 is depicted in Fig. 7. The magnetic field measurements are summarized in Table 7.

Besides the target star HD 73619, during the same nights we also observed HD 52711 and 53 Cam as non-magnetic and magnetic standard stars, respectively. For each standard star, two spectra were obtained, one per night of observation. Within the observational uncertainties, the measured values of the magnetic field in 53 Cam are con-

sistent with the published results (e.g., Hill et al. 1998; Kochukhov et al. 2004; Martínez-Arnáiz et al. 2010). Unlike the magnetic standard stars, a solar-type star such as HD 52711 should not manifest a magnetic field within the typical B_z measurement uncertainties. A spurious signal of circular polarisation in one spectrum of HD 52711 obtained during the second night, is attributable to instrumental effects.

This signal, in combination with an incomplete separation of lines in the spectrum of HD 73619, is the apparent cause for the measured negative longitudinal magnetic field of the star. To check the reliability of this result, we constructed a mask of not-blended lines belonging to the different components and measured the signal only within the mask. Taking into account this finding, we conclude that both components of the HD 73619 system do not possess a magnetic field above 200 G. Nevertheless, in light of multiple observations of the extremely weak magnetic fields seen in some Am stars, we propose additional high-resolution spectropolarimetric observations prior to any confirmation of magnetic field strengths at the sub-hundred Gauss level.

6 SURFACE ROTATION

As a part of the Nainital-Cape survey, a total of 337 Ap and Am stars were monitored to search for photometric variability and most of them turned out to be non-variables. The most plausible reason is because the light variations (if any) are of low amplitude, and thus undetectable from the ground. Using the high-precision space-based *K2* data, we confirm the presence of sub-milli-magnitude amplitude light variability in HD 73045, HD 73574, HD 73618, HD 73619, and HD 76310, which were previously classified as non-variable stars as part of the Nainital-Cape survey. In the following subsections, we discuss the possible sources of light variation.

6.1 Rotational Modulation

Rotational modulation in the light curve of a periodic variable is an indication of the presence of star spots or co-rotating clouds. The periodogram associated with rotational modulation can be characterized by the presence of harmonics of the rotation period (e.g., Santos et al. 2017). However, rotational variables may not always exhibit detectable harmonics besides the fundamental period. Therefore, at low frequencies, it becomes increasingly difficult to distinguish between binarity and rotation. Nevertheless, the amplitude of light variations due to co-rotating star spots may change in time because of spot evolution, whereas the amplitude of light variations due to orbital motion is expected to remain unchanged during the time of observation.

In order to understand the nature of low-frequency variations in A-type stars, Balona (2011) assumed that the frequency of highest amplitude in the frequency range $0.1 \text{ d}^{-1} < f < 5.0 \text{ d}^{-1}$ is the rotation frequency. There are two ways of validating that the variability is due to rotational modulation. One way is to demonstrate that there is a relationship between the projected rotational velocities, $v \sin i$, and the predicted equatorial rotational velocities, v_{rot} . Since $\sin i \leq 1$, the expectation is that in a plot of $v \sin i$ as a function of v_{rot} , all points will lie below or (less frequent) on the line $v \sin i = v_{\text{rot}}$, subject to measurement errors (Balona 2017). Another method is to show that for stars in the main-sequence band the distribution of v_{rot} , derived from the rotational frequency f_{rot} and from an estimate of the stellar radius, matches the distribution of v_{rot} derived from spectroscopic measurements of $v \sin i$ for stars in the same stellar effective temperature range (Balona 2013).

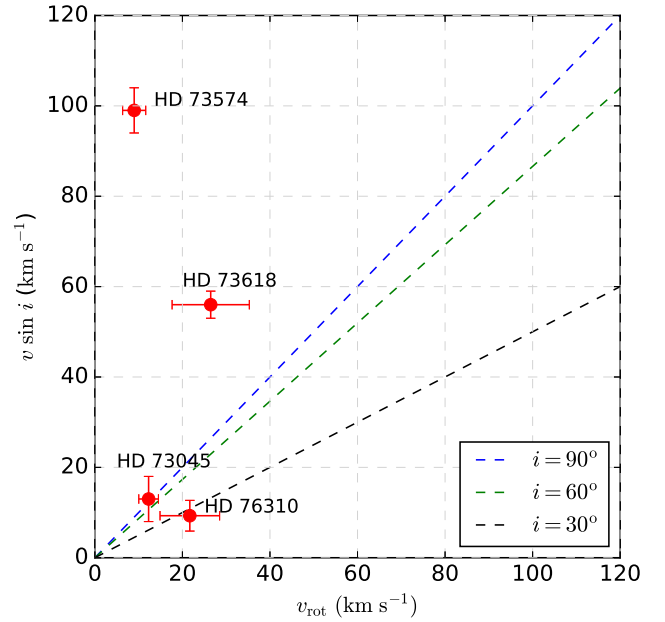


Figure 8. The projected rotational velocity $v \sin i$ as a function of predicted equatorial rotational velocity v_{rot} for the target stars. The blue, green, and black dashed lines correspond to the inclination angle $i = 90^\circ$, 60° , and 30° , respectively. Note that HD 73619 is not included in this diagram because its photometric signal is orbital in nature.

Fig. 8 shows the distribution of $v \sin i$ as a function of the v_{rot} . From this figure, it is evident that two stars, namely HD 73045 and HD 76310, are located below the line corresponding to the inclination angle $i = 90^\circ$. Therefore, the observed variations are compatible with an interpretation of spot-like features. Based on the two observations available to us, we classify HD 73045 and HD 76310 as rotational variables. For the remaining two stars, HD 73574 and HD 73618, positioned above the diagonal line, the source of variability is unknown, thus demanding further investigations. We did not include HD 73619 in Fig. 8 because its dominant signal is clearly of orbital origin.

6.2 Surface Mapping

In order to confirm the presence and locations of spots on stellar surfaces, the phased light curves were transformed into stellar images using the inversion technique developed by Savanov & Strassmeier (2008). The surface mapping was performed for HD 73045 and HD 76310, classified as rotational variables in Section 6.1. The data for the other stars contain many artefacts that are most likely spacecraft-related (the regular thruster firings to maintain pointing), hence the poor quality data prevent us to construct high-precision spot maps.

The time-series data were divided into different observational data sets, each covering one rotational period of the star. Hence, we analysed 43 and 8 data sets for HD 76310 and HD 73045, respectively. The stellar surface was divided into a grid of $6^\circ \times 6^\circ$ pixels of unit area and the values of the filling factor were determined for each grid pixel. The temperature inhomogeneity maps were constructed for inclination angle $i = 45^\circ$.

Fig. 9 shows the surface temperature inhomogeneity maps of HD 73045. There are obvious concentrations of spots at two longitudes registered as two independent spotted regions. The positions

of the spots on the surface of HD 73045 vary rapidly on time-scales of one rotational period of about 13 days. The maps clearly reveal that spots are continuously changing their location in longitudinal direction, a clear indication of rotation. For HD 76310 (Fig. C6), there is typically only one spotted region at longitudes corresponding to phases 0.5–0.7, but for the map numbers from 10 to 15, 29, 32, and 35, two spot-like structures are visible. Furthermore, the light curves become more flattened. The spot shape in most of the maps is elongated; one can also assume that for maps from 10 to 15, a single spotted region is split into two regions. This result supports our previous detailed analysis of spot activity for several Am stars (Savanov 2018) exhibiting complex behaviours depending on the positions of spots on the stellar surfaces.

6.3 Wavelet Analysis

Akin to sunspots, the star spots are well-established tracers of stellar rotation, but their dynamic behaviour may also be used to analyze other relevant phenomena, such as stability, stellar magnetic activity, and cycles (García et al. 2010; Mathur et al. 2014). Similar to sunspots, the size and location of star spots also change; sometimes they suddenly appear or vanish. One might expect the same behaviour for spots on A-type stars, leading to variations in the amplitude of the frequencies. In order to investigate the change in frequency, we constructed time–frequency diagrams for the *K2* data sets of each star based on the wavelet technique that allows a better interpretation of the physical features (such as spots) prior to their consideration for period refinement (Torrence & Compo 1998; Mathur et al. 2010).

For a given signal, this technique permits the analysis of frequency (or period) variations with time (non-stationary signals). The Morlet wavelet, which is interpreted as the convolution of a sinusoidal and a Gaussian function, was used as the reference wavelet (Goupillard et al. 1984; Holschneider et al. 1989). For a given frequency, we calculated the correlation between the mother wavelet and the data by sliding the wavelet along the time axis of the light curves, resulting in a wavelet power spectrum (WPS). The WPS was then projected on the period axis to obtain the global wavelets power spectrum (GWPS). The time–frequency plots of the studied stars are shown in Fig. 10 and Figs. C19–C28. The black and blue colours in the maps indicate regions of high and low power, respectively.

In all these cases, the variable (non-stationary) signal is noticeable. The variable signals in HD 73045 and HD 76310 could be due to the drifting of spot-like features or spot growth and decay. For HD 73574, HD 73618 and HD 73619, variable signals are detected but do not seem to be of rotational origin (spots). To confirm the nature of the signal in HD 73574, a light curve of longer timescale is required while that in HD 73618 seems to originate from the beating of close frequencies. The rotation periods (P_{GWPS}) extracted from the GWPS are 12.5 ± 1.05 d and 4.8 ± 0.45 d for HD 73045 and HD 76310, respectively. The detected periods P_{GWPS} for HD 73574, HD 73618, and HD 73619 are 14.0 ± 1.05 d, 3.8 ± 0.44 d, and $12.5/12.7 \pm 1.04$ d, respectively. The error in the periods are derived from the error in the frequencies, which are equivalent to the HWHM of the peaks in the GWPS.

6.4 Autocorrelation Function Analysis

The surface mapping and the time-frequency analysis imprint the existence and evolution of spots on the surface of rotational variables. We autocorrelated the time-series data at a given time lag to reveal the spots possibly co-rotating with the stars (McQuillan et al.

2013, 2014; García et al. 2014; Santos et al. 2019). The positive and normalised resultant autocorrelation functions (ACFs) have local maxima and minima that show the presence of spots on these stars; they mimic the displacement equation for an under-damped simple harmonic oscillator (uSHO) (Giles et al. 2017). In each ACF, the first local maximum represents the dominant period (P_{ACF}). The P_{ACF} values for HD 73045, HD 73574, HD 73618, and HD 76310 are 12.8 d, 13.5 d, 4.1 d, and 4.7 d, respectively for the *K2* C05 data. These values are in good agreement with the periods derived from the amplitude spectra, wavelet maps and composite spectra (e.g., Fig. 10, and Table 8).

The values of the spot variation time-scale (τ_{VT} ; related to the time of visibility of the spot on the stellar disk) obtained from fitting the ACF (C05) with an uSHO model are 18.67 ± 0.38 d for HD 73045 and 19.31 ± 0.13 d for HD 76310. We note, however, that the dominant frequencies in the target stars, HD 73045 and HD 76310, are sustained for a duration longer than the τ_{VT} as estimated from the ACF analysis. Santos et al. (2021) demonstrated that the *e*-folding time of the uSHO systematically underestimates the characteristic spot time-scale. Moreover, the length of the observations drastically limits the retrieved timescale (Santos et al. 2021). As a result, the length of the *K2* time-series might be insufficient to constrain spot lifetimes through the ACF. Nevertheless, we list the values for τ_{VT} , which should be considered as lower limits, and we advise caution while interpreting the retrieved τ_{VT} . The additional values of τ_{VT} obtained using the remainder of the campaigns are listed in Table 8.

Assuming that the amplitude of the rotational frequency is produced by a black circular spot, the scenario is identical to the determination of exoplanet sizes from a transit. Using *K2* C05 data for HD 73045 and HD 76310, respectively, the minimum spot radius (R_{spot}) — as derived from the photometric amplitude following a procedure described by Trust et al. (2020) — are $3.44 \pm 0.18 R_E$ and $5.04 \pm 0.27 R_E$, respectively (where R_E denotes Earth’s radius). The rest of the R_{spot} values obtained through other campaigns, when available, are given in Table 8. The τ_{VT} of the spotted regions in these stars is of the order of a few weeks. Although, as discussed above, τ_{VT} might not be a good constraint for the spot lifetimes due to the length of the observations, these results might point towards weak or non-existing magnetic fields in the program stars. The origin and nature of spots on such stars is a topic that will require detailed future modelling in consideration of that, e.g., a star like HD 73045 known to be non-magnetic (Fossati et al. 2007) shows unequivocal evidence of spots.

The composite spectrum (CS) combines the time-frequency analysis and the ACF, while being the product of the normalized GWPS and the normalized ACF (Ceillier et al. 2016, 2017). The period estimate, P_{CS} , including the respective uncertainty, corresponds to the central period and HWHM of the Gaussian function that fits the highest peak in the CS. The results from the wavelet maps, and the ACF and CS analyses are listed in Table 8.

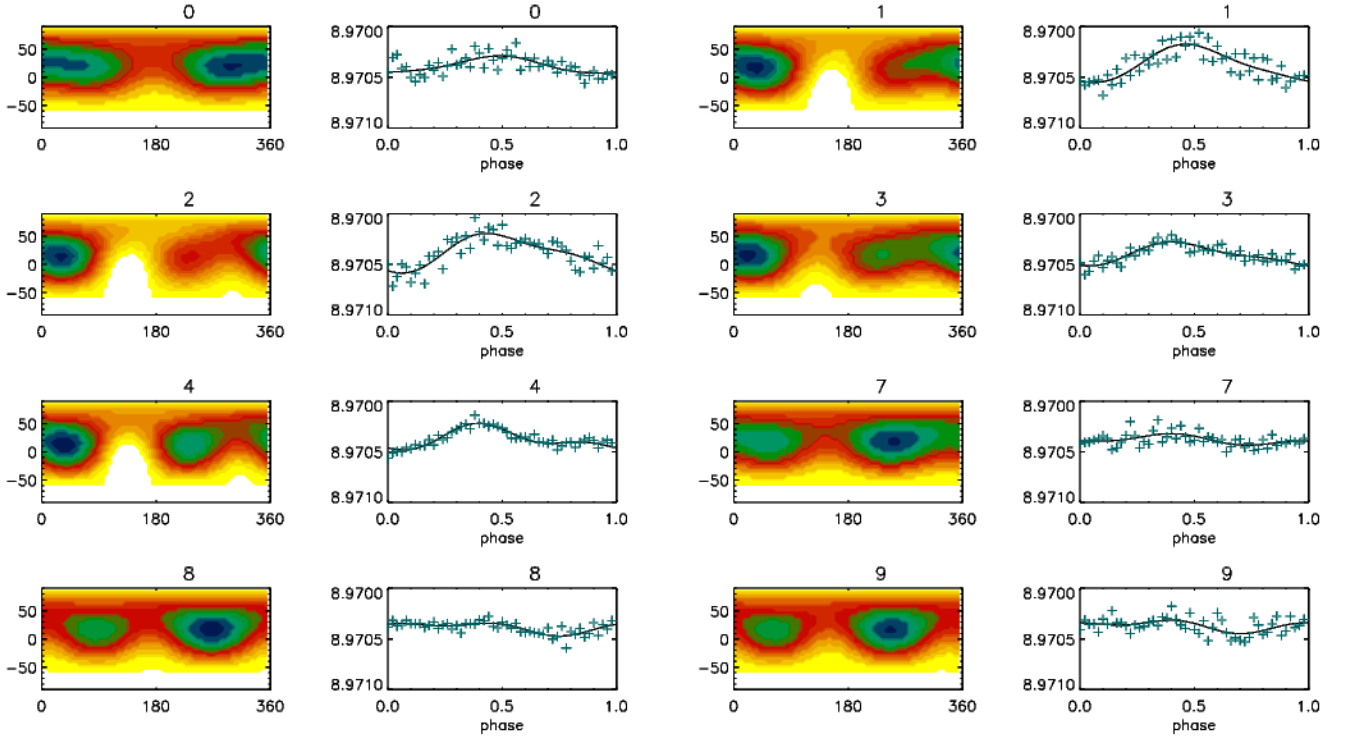


Figure 9. Temperature inhomogeneity maps of HD 73045 constructed for eight data sets. All maps use the same scale. Darker areas imply a higher spot filling factor (i.e., darkest regions correspond to a filling factor of about 0.994). The abscissa denotes the longitude in degrees and the ordinate denotes the latitude in degrees. The phase diagrams show both the observed and the model reconstructed light curves.

Table 8. The approximate spot radius (R_{spot}) as derived from the amplitude, period (P_{ACF}), and variation time-scale (τ_{VT}) as estimated from the autocorrelation functions and the rotation periods (P_{GWPS}). The composite spectrum power estimate (P_{CS}) is obtained from the respective global wavelet power spectrum and composite spectrum.

Star Name	Campaign	R_{spot} (R_{E})	P_{ACF} (d)	τ_{VT} (d)	P_{GWPS} (d)	P_{CS} (d)
HD 73045	C05	3.44 ± 0.18	12.8	18.67 ± 0.38	12.5 ± 1.04	12.7 ± 0.61
	C18	2.02 ± 0.17	12.8	16.07 ± 0.24	12.5 ± 1.05	12.8 ± 0.57
HD 73574	C05		13.5		14.0 ± 1.05	13.8 ± 0.75
HD 73618	C05		4.1		3.8 ± 0.44	3.9 ± 0.21
	C16		4.3		4.1 ± 0.44	4.3 ± 0.23
	C18		3.9		3.8 ± 0.44	3.8 ± 0.20
HD 73619	C05		12.9		12.7 ± 1.04	12.8 ± 0.50
	C18		12.8		12.5 ± 1.04	12.7 ± 0.57
HD 76310	C05	5.04 ± 0.27	4.7	19.31 ± 0.13	4.6 ± 0.45	4.7 ± 0.21
	C16	4.49 ± 0.26	4.9	18.55 ± 0.27	4.8 ± 0.45	4.9 ± 0.23
	C18	7.44 ± 0.30	4.8	21.68 ± 0.13	4.8 ± 0.45	4.8 ± 0.22

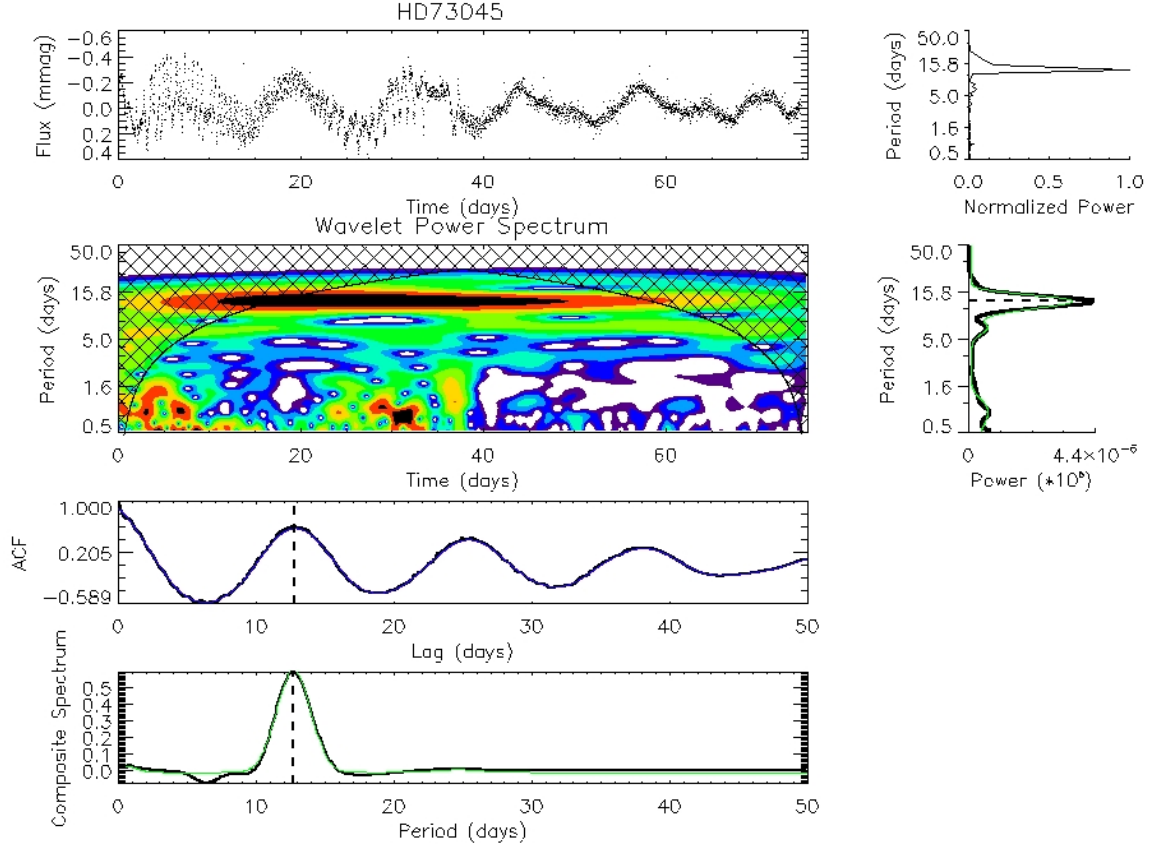


Figure 10. Wavelet map of HD 73045 using the C05 data. The top left panel shows the light curve while on the top right is the associated power density spectrum as a function of period between 0.5 and 50 d. The left panel of the second row depicts the wavelet power spectrum (WPS) computed using a Morlet wavelet between 0.5 and 50 d on a logarithmic scale and the associated global wavelet power spectrum (GWPS) is in right panel of the second row. The black and blue colours correspond to high and low power, respectively. The black-crossed area is the cone of influence corresponding to the unreliable results. The panel on the third row shows the autocorrelation function (ACF) of the full light curve plotted between 0 and 50 d. Finally, the composite spectrum (Ceillier et al. 2016, 2017) is shown in the bottom panel. The black dashed lines mark the respective rotation period estimates.

7 AN OBSERVATIONAL H-R DIAGRAM

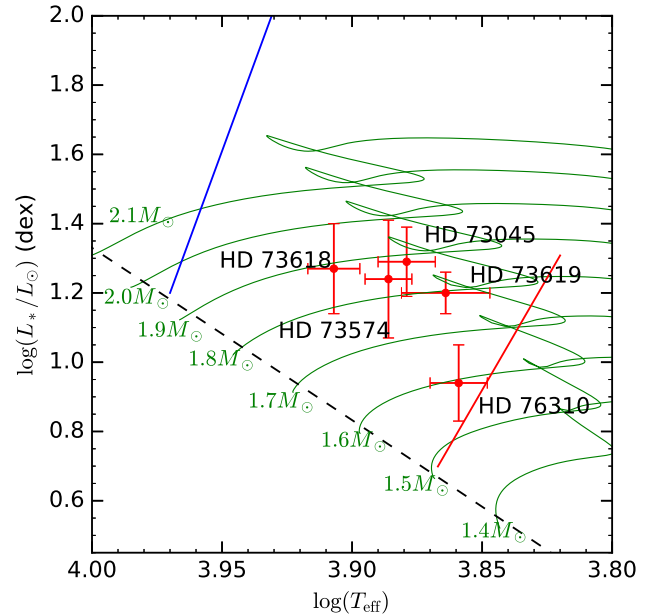


Figure 11. Location of the target stars in the H-R diagram. The solid green lines represent the theoretical evolutionary tracks for the masses from $1.4 M_{\odot}$ to $2.1 M_{\odot}$ taken from [Murphy et al. \(2019\)](#). The blue and red edges of the observational δ Scuti instability strip are over-plotted with blue and red lines, respectively. The black dashed line represents the ZAMS.

high-resolution spectroscopy allows to deduce accurate values of T_{eff} and $\log(L_{\star}/L_{\odot})$ as this method takes into account line blanketing caused by the chemical peculiarities.

The values of $\log(L_{\star}/L_{\odot})$ of the programme stars have been calculated using the standard relation as discussed in [Balona \(2018\)](#). The bolometric corrections for the Sloan Digital Sky Survey (SDSS) ugriz photometric system were obtained from [Girardi et al. \(2004\)](#). For the derivation of the absolute magnitude, the *Gaia* EDR3 parallaxes ([Gaia Collaboration et al. 2021](#)) were used. Combining all these values yielded adequate $\log(L_{\star}/L_{\odot})$ values, which are presented in Table 6.

Based on the derived T_{eff} and $\log(L_{\star}/L_{\odot})$ values, we placed the programme stars in the H-R diagram and their location is shown in Fig. 11. On inspection of their position, we conclude that all stars moved away from the ZAMS and are heading towards the Terminal Age Main Sequence (TAMS). Considering the error boxes, all targets lie within the δ Scuti observational instability strip as determined by [Murphy et al. \(2019\)](#).

8 COMMENTS ON INDIVIDUAL STARS

Capitalizing on the unprecedented quality of photometric data obtained from space missions, searches for photometric variability followed by determinations of the various stellar physical properties using high-resolution spectroscopy help us to ascertain the various stellar properties and activities such as chemical peculiarities, spots, pulsation, and rotation. The following subsections provide a brief summary and discussion about individual stars along with information on their basic physical properties.

In order to infer the evolutionary status, the location of the target stars within the H-R diagram needs to be precisely determined. Therefore, accurate values for the effective temperature T_{eff} and the luminosity L_{\star} need to be obtained; note that a typical error of 150 K in T_{eff} (as given by many traditional methods) entails an error of about 0.2 mag in the bolometric magnitude ([Neiner & Lampens 2015](#)). Fortunately,

8.1 HD 73045/KW 538 (Praesepe)

HD 73045 is classified as an Am star by [Bidelman \(1956\)](#) and [Bertaud \(1960\)](#) with a spectral type A7.2 ([Kraus & Hillenbrand 2007](#)) and classified as an SB1 ([Debernardi et al. 2000](#); [Carquillat & Prieur 2007](#)). This star was extensively studied by [Fossati et al. \(2007, 2008\)](#) who derived the basic physical parameters, chemical composition. They reported that the star is of non-magnetic nature.

HD 73045 was photometrically analysed using the HI-1A photometer of the Heliospheric Imager ([Eyles et al. 2009](#)) aboard the STEREO spacecraft ([Driesman et al. 2008](#)) — a study done by [Paunzen et al. \(2013\)](#) who reported a variability period of 1.25 d. However, this variation was a consequence of the pixel response function (PRF) of HD 73045 blending with that of its visual neighbor BD+19°2046 (P. E. Williams, 2019, private communication). The blended PRFs vary in shape and periodically bleed outside of the circular collection aperture as the sources track across the instrument’s field-of-view. The sources were found to shift from one y -pixel to the next with a period of 1.25 d, coinciding with the period reported by [Paunzen et al. \(2013\)](#). Our analysis did not find any evidence for a periodicity of 1.25 d in the long cadence as well as the short cadence K2 data, hence contradicting the findings of the variability of 1.25 d reported by [Paunzen et al. \(2013\)](#).

Applying the analyses described in Section 2.2 to the LC K2 data, the photometric variation exhibits a dominant component close to 12.65 d (12.68 d for C05 and 12.64 d for C18). Both data sets also show similar secondary signals at 6.42 d and 6.51 d, respectively. The WPS and GWPS (Fig. 10) also shows an excess of power at around the half of the dominant period. These secondary signals are close to harmonics of the dominant components. However, they do not correspond exactly to harmonics as can be seen in the irregular characteristic of the light curve, highlighted by the models (e.g., Fig. 3, top-left, red), whereas a harmonic signal would exhibit a repetitive period-to-period structure. This observed feature is also visible in other stars such as HD 174356 ([Bowman et al. 2018](#)) and, with more complexity, in Atlas in the Pleiades ([White et al. 2017](#)). Based on the surface map, time-frequency and the ACF analyses, the origin of the periodic variability in HD 73045 could be attributable to star spots situated at different latitudes on a star exhibiting differential rotation. Particularly, the rotational modulation in Fig. 3 shows a double dip feature which indicates the presence of at least two dominant spots.

Analysing the C18 SC data (Fig. C8, top), the two main components described above are observed. The main goal in studying these data, however, was to confirm short-term variability (i.e., 16, 28.8, and 36 d⁻¹) as previously suspected by [Joshi et al. \(2015\)](#). However, as revealed in the Lomb-Scargle spectral frequency distribution (Fig. C8, bottom), the range of interest (as shown in the inset) exhibits no clear signals above the noise level that would meet the FAP threshold criterion. In addition, the time-resolved radial velocity analysis did not reveal any short-term variability. Therefore, within the given photometric and spectroscopic detection limits, we conclude that HD 73045 is pulsationally stable. The RV values derived from our observations agrees well with the previous measurements by [Carquillat & Prieur \(2007\)](#). Indeed, the radial velocities, after being averaged over each series, are in good agreement with theoretical predictions based on the published stellar orbital parameters.

8.2 HD 73574/KW 203 (Praesepe)

HD 73574 is classified as A5V and A5III by [Bidelman \(1956\)](#) and [Rebeiro \(1966\)](#), respectively. [Fossati et al. \(2008\)](#) determined the values for T_{eff} , $\log g$ and $[F_e/H]$ as 7662 K, 4.00 (cgs) and 0.10,

respectively. This star was identified as a moderate rotator with $v \sin i$ of 120 km s⁻¹ ([McGee et al. 1967](#)). The K2 C05 data set exhibits two periods, namely, 10.8 d and 14.27 d (see Fig. C9). From the time-frequency as well as the ACF and CS analyses of the K2 C05 data set, it is found that HD 73574 shows a periodicity of about 13.8 d (Fig. C20).

Using the spectroscopic observations, we derived values of T_{eff} , $\log g$, $[M/H]$, ξ , $v \sin i$ and RV as 7700 ± 160 K, 4.12 ± 0.21 (cgs), 0.07 ± 0.11 , 2.12 ± 0.17 km s⁻¹, 99 ± 5 km s⁻¹, and 29.2 ± 2.8 km s⁻¹, respectively.

8.3 HD 73618/KW 224 (Praesepe)

HD 73618 is classified as A0 spectral type ([Cannon & Pickering 1993](#)). It is also referred to as an Am star ([Bidelman 1956](#); [Bertaud 1960](#); [Rebeiro 1966](#)). The $v \sin i$ value for this star was reported as 51 km s⁻¹ ([Abt & Willmarth 1999](#)) and 44 km s⁻¹ ([Debernardi et al. 2000](#)).

[Mason et al. \(1993\)](#) identified this star as the primary component of a SB1 binary system in which the flux of the secondary star does not significantly influence the combined total flux spectrum. There are various studies about the atmospheric parameters. Based on those determinations, T_{eff} , $\log g$, and $[F_e/H]$ are given as 8060 K, 3.87 (cgs), and 0.46 by [Hui-Bon-Hoa et al. \(1997\)](#), 8100 K, 4.00 (cgs), and 0.50 by [Burkhart & Coupry \(1998\)](#), and 8170 K, 4.00 (cgs), and 0.46 by [Fossati et al. \(2007\)](#), respectively. [Fossati et al. \(2007\)](#) did not find any detectable magnetic field.

The K2 C05 data set (Fig. C11) shows a dominant peak at 3.78 d. In the C16 data set (Fig. C12), the three peaks are given as 3.83 d, 4.87 d, and 2.49 d, whereas in the C18 data set (Fig. C13), they are given as 3.76 d, 4.81 d, and 2.37 d. These main features are accompanied by lower amplitude, seemingly unrelated, components, producing a rather complex time-series. The time-frequency, ACF and CS analyses suggest a periodic variability of about 4 d with its origin still undetermined.

An attempt was made to analyse the C16 and C18 time-series together, in a ~208-day dataset that includes a non-centered gap extending across 36 per cent of the temporal baseline. While issues arise when applying Fourier methods to gapped data ([Munteanu et al. 2016](#)), the Lomb-Scargle algorithm did produce a periodogram with a frequency resolution of 0.05 d⁻¹. Applying oversampling to the Lomb-Scargle process introduced sidelobes that completely corrupting the periodogram.

Based on our spectroscopic analysis, the derived parameters are given as $T_{\text{eff}} = 7960 \pm 180$ K, $\log g = 3.76 \pm 0.19$ (cgs), $[M/H] = 0.34 \pm 0.11$, $\xi = 2.77 \pm 0.16$ km s⁻¹, $v \sin i = 56 \pm 3$ km s⁻¹, and RV = 39.5 ± 0.5 km s⁻¹. Based on age and metallicity, [Ahumada & Lapasset \(2007\)](#) classified HD 73618 as a blue straggler; hence, it can be considered an ideal object for testing current models of collisionally formed blue stragglers. The wide and detailed knowledge available on this star and its environment should allow us to test the reliability of current models and provide important constraints for future model development.

8.4 HD 73619/KW 229 (Praesepe)

HD 73619 is a member of the Praesepe open cluster ([Sanford 1931](#)). [Bidelman \(1956\)](#) identified this star as a classical Am star, with a spectral type given as A4 and F0 III based on Ca II K and metallic lines, respectively. [Abt & Willmarth \(1999\)](#) and [Debernardi et al. \(2000\)](#) identified the projected stellar rotational velocity as 20 and 11.2 km s⁻¹, respectively.

The light curve of HD 73619 shown in the upper-left panel of Fig. C14 is similar to that of a heartbeat star (Thompson et al. 2012; Fuller 2017; Hambleton et al. 2018; Wheeler & Kipping 2019; van Kooten et al. 2020). Analysis of the frequency spectrum provided orbital periodicities of 12.97 and 12.91 d from the C05 and C18 data, respectively. These values were confirmed by using time-domain autocorrelation and box fitting (Kovács et al. 2002) methods. Although HD 73619 was observed during Campaign 16 of the *K2* mission, its image was blended with HD 73598; thus, these C16 observations have been excluded from this study.

A thorough search for any pulsational variability induced by tidal interaction requires an accurate model to be constructed and subtracted from the light curve, and the residuals analysed. While conservative sinusoidal models were produced from a limited number of components (Table 3), many more components would be required to reconstruct accurately the light curve. None of these components relate to pulsational signals. Construction of a detailed model was also attempted using the PHOEBE package (Prša & Zwitter 2005), but the procedure failed to converge. However, two other methods were performed to probe the existence of pulsational phenomena.

One method involved separating the heartbeat light curve into separate intra-period segments. Each segment was fit with an eighth-order polynomial, which was subsequently subtracted from the data, resulting in respective sets of residuals (Fig. 12, top left). These residual data-sets were analysed with the LS algorithm to produce a frequency spectrum (Fig. 12, top right). While an instrumental artifact appeared in the third and fourth segments of the C05 data, neither evidence of pulsation was observed nor any such evidence was seen in the C18 data (Fig. C29). The other method involved using the K2SC algorithm previously applied to clean SAP light curves. This process also produced a de-trended residual data-set with the dominant heartbeat signal removed (Fig. 12, middle). Again, the data-sets were analysed using the LS algorithm with no evidence of pulsation signals neither in the C05 (Fig. 12, bottom) nor the C18 (Fig. C29, middle and bottom) found. In conclusion, within the limits of our analysis, HD 73619 shows no evidence of pulsational variability.

Based on the parameters given in Table 5, we ratify that the two components of the heartbeat system have similar characteristics. From Fig. 4, our revised radial velocities support the orbital solution determined by Debernardi et al. (2000). Moreover, Debernardi et al. (2000) reported an orbital period of 12.91124 ± 0.00004 d. This implies that the dominant 12.91 d signal detected in both *K2* data sets is orbital in nature. The spectropolarimetric analysis indicates that, within the observational uncertainty of 200 G, magnetic fields in HD 73619 are either weak or absent.

8.5 HD 76310

Cowley & Cowley (1965b) classified HD 76310 as an Am star. The projected rotational velocity $v \sin i$ as a function of the predicted equatorial rotational velocity v_{rot} for the target stars. The blue, green, and black dashed lines correspond to the inclination angle $i = 90^\circ$, 60° , and 30° , respectively. Note that HD 73619 is not included in this diagram because its photometric signal is orbital in nature.

All three *K2* data sets tend to be dominated by two components at ~ 4.7 d and ~ 5.4 d, with variation around those values across the campaigns. These close frequencies result in well-pronounced beating effects in C05 (Fig. C16) and C16 (Fig. C17), but less interaction between the components during C18 (Fig. C18) where the shape of the time-series varies across the periods. The level of these interactions are defined by the ratio of their amplitudes. Also note that

overtone of the ~ 4.8 d feature seem to exist, although they do not always clear the FAP threshold and, in some cases, are obscured by the background noise. Finally, it is noteworthy that the modeling of the C05 time-series failed to produce a good fit to the data when the single component relating to the dominant 4.622 d peak was included, and two other components at around ± 0.3 d either side of the peak were required to better fit the data. From the time-series analysis of the *K2* data, the surface map, the wavelet, the ACF, and the composite spectrum, a dominant period close to 4.7 d was obtained. Given that the photometric amplitude of HD 73610 changes significantly within only a few dozen variability cycles, we may not rule out the possibility of having unresolved multiperiodic pulsational signals, for instance of the γ Doradus type. An attempt to analyse the combined time-series of C16 and C18, corresponding to that for HD 73618, was performed with a similar outcome.

On investigating the $v \sin i$ vs. v_{rot} diagram in Fig. 8, HD 76310 was found to be positioned below the line of $\sin i = 1$. Based on the surface maps, wavelet, and ACF, we thus categorise this star as a rotational variable. The LSD profiles shown in Fig. 13 indicate a complex structure. The RV values obtained at different epochs (December 2018 and April 2020) are the same within the observational uncertainty (i.e., $20.13 \pm 0.40 \text{ km s}^{-1}$ and $20.22 \pm 0.83 \text{ km s}^{-1}$, respectively). The similarity between the shapes of the LSD profile of HD 76310 and the CCF profile of KIC 11572666 (Lampens et al. 2018) implies that the system is an SB2 system. We fitted the MRES spectrum of HD 76310 with a composite model using the 2D version of GIRFIT in spectral regions around H_γ (430–440 nm), H_β (470–500 nm), H_α (630–680 nm), and the Mg I triplet (510–520 nm). We treated the component T_{eff} , $v \sin i$, RV and the luminosity ratio as free parameters while keeping $\log g$ fixed at 4.0 (cgs).

The composite spectrum was fitted well (e.g., see H_β line in Fig. 14); thus, we adopted the mean values of the stellar parameters from these spectral regions. The obtained values are: effective temperature of $T_{\text{eff}1} = 7030 \pm 170 \text{ K}$ and $T_{\text{eff}2} = 6470 \pm 220 \text{ K}$, $v \sin i$ of $97.1 \pm 0.4 \text{ km s}^{-1}$ and $9.3 \pm 0.7 \text{ km s}^{-1}$, RV of $27.4 \pm 1.8 \text{ km s}^{-1}$ and $19.8 \pm 2.8 \text{ km s}^{-1}$, respectively, with a light ratio I_1 of 0.887 ± 0.023 (see Table 5).

Based on the rotational velocities and periods of HD 76310, the source of the stellar photometric variability, as indicated, could be the sharp-lined and cooler component, thus favouring the stellar binarity hypothesis. It is also noteworthy that HD 76310 is included in the Washington Double Star Catalogue (Mason et al. 2001) as a system consisting of two equally bright stars separated by 0.1 arcsec. Nevertheless, there is still the possibility that HD 76310 is a single star surrounded by a cloud shell (Slettebak 1986; Fekel et al. 2003). Future observations would be crucial for exploring the variability and possible binarity nature of this object (Welsh & Montgomery 2013).

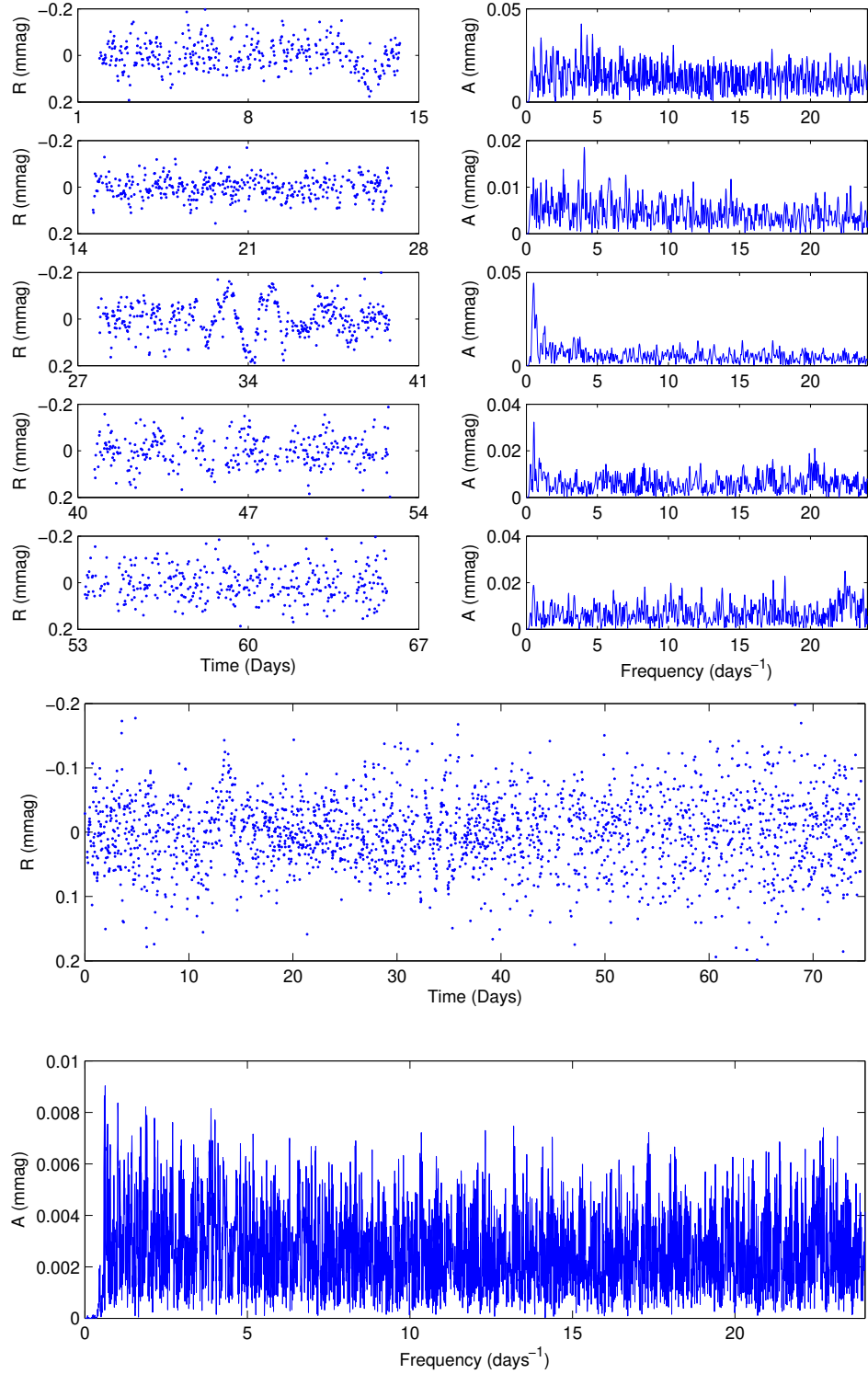


Figure 12. The top five rows illustrate the residual light curve (left) and amplitude spectrum (right) of HD 73619 after removing the heartbeat signal from five segments of the C05 time-series. The $\sim 0.5 \text{ d}^{-1}$ spectral peak in segments 3 and 4 are related to an instrumental artifact. The middle panel shows the complete time-series after being de-trended by the k2sc algorithm with its respective amplitude spectrum in the bottom panel. Neither analysis indicates any evidence for the existence of pulsation phenomena.

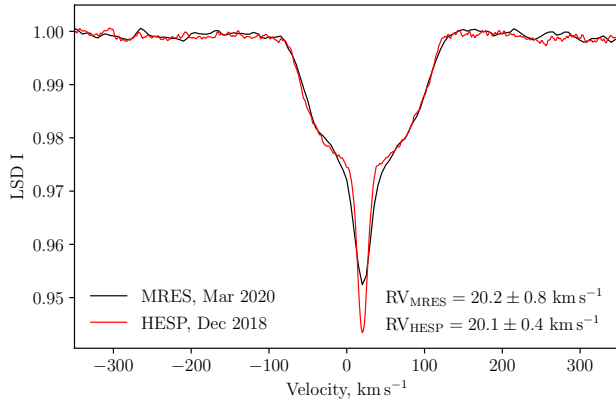


Figure 13. The LSD profiles for HD 76310 based on HESP (red) and MRES (black) data.

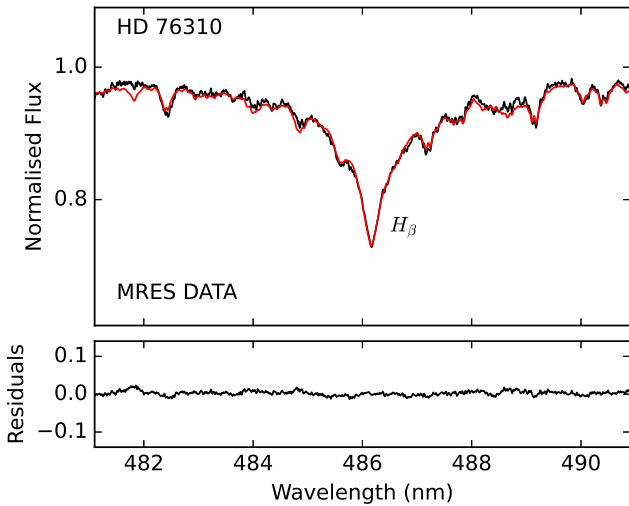


Figure 14. The H_β MRES spectrum for HD 76310 (black) and the composite model spectrum (red) obtained using the 2D version of GIRFIT.

9 CONCLUSIONS AND FUTURE PROSPECTS

Based on the time-series photometry obtained from the ground, the *K2* mission and from contemporaneous high-resolution spectroscopy and spectropolarimetry, we arrived at the following conclusions:

- All targets in the study sample, previously part of the Nainital-Cape survey and classified as constant stars, are now (potentially) identified as variables. Our analysis suggests that HD 73045 and HD 76310 are rotational variables. The LSD profiles of HD 76310 indicates that this star is part of binary system or surrounded by a cloud shell. The light variation recorded for HD 73619 is consistent with orbital signals and likely to be the first chemically peculiar Am star in a heartbeat system without tidally induced pulsations. As we could not ascertain the origin of the variability of HD 73574 and HD 73618, further time-domain studies are needed to apprehend the nature of these objects.

- Within the detection limits of the *K2* photometry and radial velocity measurements, we conclude that HD 73045 is pulsationally stable contrary to the previous prediction by Joshi et al. (2015). Simi-

larly, the analysis of the *K2* data revealed the absence of a periodicity of 1.25 d previously reported by Paunzen et al. (2013); it is confirmed as previously erroneous.

- High-resolution spectroscopy measurements obtained with two spectrographs at different epochs revealed that the HD 73619 system is comprised of two stars with similar properties. The individual radial velocities of HD 73619 at the different epochs are in good agreement with the orbital solution by Debernardi et al. (2000). The spectropolarimetric data analysis indicates that HD 73619 may possess a weak magnetic field, hence additional high-resolution spectropolarimetric observations would be essential for confirmation.

- The atmospheric parameters of the target stars have been derived using high-resolution spectroscopy. Considering observational uncertainties, it is found that all the studied stars are evolved away from the ZAMS and located within the δ Scuti instability strip.

The potential presence of a weak magnetic field in HD 73619, and the surface spots seen on HD 73045 and HD 76310, constitute further evidence that magnetic fields cannot be disregarded when exploring the origin of the peculiar chemical abundances in Am stars. The magnetic fields leading to the formation of the surface spots might not be stable, suggesting that they may be dominated by the dynamo effect. It is unclear if (or how) magnetic fields would affect the diffusion model for the formation of the peculiar chemical abundances in these stars, or whether alternative formation mechanism(s) would be needed to explain these phenomena.

The origin of weak magnetic fields in metallic line (Am) stars and even in normal δ Sct stars (hotter than Sun) are fossil or related to a dynamo effect is still largely an unsolved problem, although copious valuable contributions for A-type stars have previously been made (e.g., MacDonald & Mullan 2004). A detailed study of the various underlying processes, particularly the diverse theoretical aspects require more attention. Future studies are relevant to the bigger picture of stellar and galactic evolution, in consideration of the significance of massive stars, notably for the production and proliferation of heavy elements as well as the overall galactic chemistry (e.g., Matteucci 2021, and references therein).

Our overall long-term goal of this work is to continue the study of stellar structure and atmospheres of CP stars as well as of magnetic fields, inhomogeneities (such as spots), and tidal interaction. In the framework of our ongoing research, our future plan is to extend the detailed analysis of heretofore unstudied CP stars with *TESS* data in combination with future high-resolution spectroscopic and spectropolarimetric observations.

ACKNOWLEDGMENTS

The work presented here is supported by the Belgo-Indian Network for Astronomy and astrophysics (BINA), sanctioned by Department of Science and Technology (DST, Govt. of India; DST/INT/Belg/P-09/2017) and the Belgian Federal Science Policy Office (BELSPO, Govt. of Belgium; BL/33/IN12). OT and EJ thank the International Science Programme (ISP) of Uppsala University and African Astronomical Society (AfAS) for financial support. DLH acknowledges financial support from the Science and Technology Facilities Council (STFC) via grant ST/M000877/1. AG, DM, and SJ are grateful for the support received from the Indo-Thailand Programme of co-operation in Science and Technology through the Indo-Thai joint project DST/INT/Thai/P-16/2019. FKA and SC thanks the Polish National Center for Science (NCN) for grant 2015/18/A/ST9/00578. RAG acknowledges support from the CNES PLATO grant. SM acknowledges support from the Spanish Ministry with the Ramon

Cajal fellowship number RYC-2015-17697. ARGs acknowledges support from NASA under Grant No. NNX17AF27G and from STFC consolidated grant ST/T000252/1. IS thanks the Government of the Russian Federation and the Ministry of Higher Education and Science of the Russian Federation, grant no. 075-15-2020-780 (N13.1902.21.0039). This paper includes data collected by the *K2* mission available at Mikulski Archive for Space Telescopes (MAST), SIMBAD and NASA's ADS. The authors thank the anonymous reviewer for the insightful comments and suggestions which led to the improvement of the manuscript.

DATA AVAILABILITY

The data underlying this article will be shared on reasonable request to the corresponding author.

REFERENCES

- Abt H. A., Willmarth D. W., 1999, *ApJ*, **521**, 682
- Ahumada J. A., Lapasset E., 2007, *A&A*, **463**, 789
- Aigrain S., Hodgkin S. T., Irwin M. J., Lewis J. R., Roberts S. J., 2015, *MNRAS*, **447**, 2880
- Aigrain S., Parviainen H., Pope B. J. S., 2016, *MNRAS*, **459**, 2408
- Antoci V., et al., 2019, *MNRAS*, **490**, 4040
- Ashoka B. N., et al., 2000, *Bulletin of the Astronomical Society of India*, **28**, 251
- Asplund M., Grevesse N., Sauval A. J., Scott P., 2009, *ARA&A*, **47**, 481
- Bagnulo S., Szeifert T., Wade G. A., Landstreet J. D., Mathys G., 2002, *A&A*, **389**, 191
- Balona L. A., 2011, *MNRAS*, **415**, 1691
- Balona L. A., 2013, *MNRAS*, **431**, 2240
- Balona L. A., 2017, *MNRAS*, **467**, 1830
- Balona L. A., 2018, *Monthly Notices of the Royal Astronomical Society*, **479**, 183
- Balona L. A., Catanzaro G., Abedigamba O. P., Ripepi V., Smalley B., 2015, *MNRAS*, **448**, 1378
- Beck P. G., et al., 2014, *A&A*, **564**, A36
- Bertaud C., 1960, *Journal des Observateurs*, **43**, 129
- Bidelman W. P., 1956, *PASP*, **68**, 318
- Blanco-Cuaresma S., 2019, arXiv e-prints,
- Blanco-Cuaresma S., Soubiran C., Jofré P., Heiter U., 2014, in *Astronomical Society of India Conference Series*. pp 85–91 ([arXiv:1312.4545](https://arxiv.org/abs/1312.4545))
- Blazère A., et al., 2015, in *Nagendra K. N., Bagnulo S., Centeno R., Jesús Martínez González M., eds, IAU Symposium Vol. 305, Polarimetry*. pp 67–72, [doi:10.1017/S1743921315004536](https://doi.org/10.1017/S1743921315004536)
- Blazère A., Neiner C., Petit P., 2016, *MNRAS*, **459**, L81
- Böhm T., et al., 2015, *A&A*, **577**, A64
- Bowman D. M., Buysschaert B., Neiner C., Pápics P. I., Oksala M. E., Aerts C., 2018, *A&A*, **616**, A77
- Breger M., et al., 1993, *A&A*, **271**, 482
- Burdanov A. Y., Krushinsky V. V., Popov A. A., 2014, *Astrophysical Bulletin*, **69**, 368
- Burkart J., Quataert E., Arras P., Weinberg N. N., 2012, *MNRAS*, **421**, 983
- Burkhart C., Coupry M. F., 1998, *A&A*, **338**, 1073
- Cannon A. J., Pickering E. C., 1993, *VizieR Online Data Catalog*, **p. III/135A**
- Carquillat J.-M., Prieur J.-L., 2007, *MNRAS*, **380**, 1064
- Castelli F., Kurucz R. L., 2003, in *Piskunov N., Weiss W. W., Gray D. F., eds, IAU Symposium Vol. 210, Modelling of Stellar Atmospheres*. p. A20
- Ceillier T., et al., 2016, *MNRAS*, **456**, 119
- Ceillier T., et al., 2017, *A&A*, **605**, A111
- Chanumolu A., Jones D., Thirupathi S., 2015, *Experimental Astronomy*, **39**, 423
- Choutonov G. A., 2004, in *Arkhyz N., Glagolevskij Y. V., Kudryavtsev I. I., Romanyuk I. I., eds, Magnetic Stars*. pp 286–291
- Cowley A. P., Cowley C. R., 1965a, *PASP*, **77**, 184
- Cowley A. P., Cowley C. R., 1965b, *Publications of the Astronomical Society of the Pacific*, **77**, 184
- Crawford D. L., Mandwewala N., 1976, *PASP*, **88**, 917
- Cutri R. M., et al., 2003, *VizieR Online Data Catalog*, **p. II/246**
- Davis L. E., 1994, A reference guide to the iraf/daophot package, <http://citeseerx.ist.psu.edu/viewdoc/download?doi=10.1.1.584.2658&rep=rep1&type=pdf>
- Debernardi Y., Mermilliod J.-C., Carquillat J.-M., Ginestet N., 2000, *A&A*, **354**, 881
- Driesman A., Hynes S., Cancro G., 2008, *Space Sci. Rev.*, **136**, 17
- Eyles C. J., et al., 2009, *Sol. Phys.*, **254**, 387
- Fekel F. C., Warner P. B., Kaye A. B., 2003, *AJ*, **125**, 2196
- Fossati L., Bagnulo S., Monier R., Khan S. A., Kochukhov O., Landstreet J., Wade G., Weiss W., 2007, *A&A*, **476**, 911
- Fossati L., Bagnulo S., Landstreet J., Wade G., Kochukhov O., Monier R., Weiss W., Gebran M., 2008, *A&A*, **483**, 891
- Frémat Y., Neiner C., Hubert A. M., Floquet M., Zorec J., Janot-Pacheco E., Renan de Medeiros J., 2006, *A&A*, **451**, 1053
- Frescura F. A. M., Engelbrecht C. A., Frank B. S., 2008, *MNRAS*, **388**, 1693
- Fuller J., 2017, *MNRAS*, **472**, 1538
- Fuller J., Lai D., 2012, *MNRAS*, **420**, 3126
- Gaia Collaboration 2018, *VizieR Online Data Catalog*, **p. I/345**
- Gaia Collaboration et al., 2021, *A&A*, **649**, A1
- García R. A., Mathur S., Salabert D., Ballot J., Régulo C., Metcalfe T. S., Baglin A., 2010, *Science*, **329**, 1032
- García R. A., et al., 2014, *A&A*, **572**, A34
- Giles H. A. C., Collier Cameron A., Haywood R. D., 2017, *MNRAS*, **472**, 1618
- Girardi L., Grebel E. K., Odenkirchen M., Chiosi C., 2004, *A&A*, **422**, 205
- Goupillaud P., Grossmann A., Morlet J., 1984, *Geoexploration*, **23**, 85
- Green G. M., 2018, *JOSS*, **3**, 695
- Green G. M., Schlafly E. F., Zucker C., Speagle J. S., Finkbeiner D. P., 2019, arXiv e-prints, [p. arXiv:1905.02734](https://arxiv.org/abs/1905.02734)
- Guo Z., Gies D. R., Fuller J., 2017, *ApJ*, **834**, 59
- Guo Z., Shporer A., Hambleton K., Isaacson H., 2020, *ApJ*, **888**, 95
- Guzik J. A., 2021, *Frontiers in Astronomy and Space Sciences*, **8**, 55
- Hambleton K. M., et al., 2013, *MNRAS*, **434**, 925
- Hambleton K., et al., 2016, *MNRAS*, **463**, 1199
- Hambleton K., et al., 2018, *MNRAS*, **473**, 5165
- Handler G., et al., 2002, *MNRAS*, **333**, 262
- Heiter U., et al., 2015, *Phys. Scr.*, **90**, 054010
- Hill G. M., Bohlender D. A., Landstreet J. D., Wade G. A., Manset N., Bastien P., 1998, *MNRAS*, **297**, 236
- Høg E., et al., 2000, *A&A*, **355**, L27
- Holschneider M., Kronland-Martinet R., Morlet J., Tchamitchian P., 1989, in *Combes J.-M., Grossmann A., Tchamitchian P., eds, Wavelets. Time-Frequency Methods and Phase Space*. p. 286
- Howell S. B., et al., 2014, *PASP*, **126**, 398
- Hui-Bon-Hoa A., Burkhart C., Alecian G., 1997, *A&A*, **323**, 901
- Joshi S., et al., 2003, *MNRAS*, **344**, 431
- Joshi S., Mary D. L., Martinez P., Kurtz D. W., Girish V., Seetha S., Sagar R., Ashoka B. N., 2006, *A&A*, **455**, 303
- Joshi S., Mary D. L., Chakradhari N. K., Tiwari S. K., Billaud C., 2009, *A&A*, **507**, 1763
- Joshi S., Ryabchikova T., Kochukhov O., Sachkov M., Tiwari S. K., Chakradhari N. K., Piskunov N., 2010, *MNRAS*, **401**, 1299
- Joshi S., et al., 2012, *MNRAS*, **424**, 2002
- Joshi S., Joshi G. C., Joshi Y. C., Aggarwal R., 2015, in *Meynet G., Georgy C., Groh J., Stee P., eds, IAU Symposium Vol. 307, New Windows on Massive Stars*. pp 218–219, [doi:10.1017/S1743921314006772](https://doi.org/10.1017/S1743921314006772)
- Joshi S., et al., 2016, *A&A*, **590**, A116
- Joshi S., Semenko E., Moiseeva A., Sharma K., Joshi Y. C., Sachkov M., Singh H. P., Yerra B. K., 2017, *MNRAS*, **467**, 633
- Kirk B., et al., 2016, *AJ*, **151**, 68
- Kochukhov O., Bagnulo S., Wade G. A., Sangalli L., Piskunov N., Landstreet J. D., Petit P., Sigut T. A. A., 2004, *A&A*, **414**, 613
- Kochukhov O., Makaganiuk V., Piskunov N., 2010, *A&A*, **524**, A5

- Kołodziejczyk-Szymański P. A., Pigulski A., Michalska G., Moździerski D., Różański T., 2020, arXiv e-prints, [p. arXiv:2012.11559](https://arxiv.org/abs/2012.11559)
- Kovács G., Zucker S., Mazeh T., 2002, *A&A*, **391**, 369
- Kraus A. L., Hillenbrand L. A., 2007, *AJ*, **134**, 2340
- Kudryavtsev D. O., Romanyuk I. I., Elkin V. G., Paunzen E., 2006, *MNRAS*, **372**, 1804
- Kumar P., Ao C. O., Quataert E. J., 1995, *ApJ*, **449**, 294
- Kupka F., 2003, in Balona L. A., Henrichs H. F., Medupe R., eds, *Astronomical Society of the Pacific Conference Series Vol. 305, Magnetic Fields in O, B and A Stars: Origin and Connection to Pulsation, Rotation and Mass Loss*. p. 190
- Lampens P., et al., 2018, *A&A*, **610**, A17
- Lipunov V., et al., 2010, *Advances in Astronomy*, **2010**, 349171
- Lomb N. R., 1976, *Ap&SS*, **39**, 447
- MacDonald J., Mullan D. J., 2004, *MNRAS*, **348**, 702
- Maceroni C., et al., 2009, *A&A*, **508**, 1375
- Martínez-Arnáiz R., Maldonado J., Montes D., Eiroa C., Montesinos B., 2010, *A&A*, **520**, A79
- Martínez P., et al., 2001, *A&A*, **371**, 1048
- Mason B. D., Hartkopf W. I., McAlister H. A., Sowell J. R., 1993, *AJ*, **106**, 637
- Mason B. D., Wycoff G. L., Hartkopf W. I., Douglass G. G., Worley C. E., 2001, *AJ*, **122**, 3466
- Mathur S., et al., 2010, *A&A*, **511**, A46
- Mathur S., et al., 2014, *A&A*, **562**, A124
- Matteucci F., 2021, *A&ARv*, **29**, 5
- McGee J. D., Khogali A., Baum W. A., Kraft R. P., 1967, *MNRAS*, **137**, 303
- McQuillan A., Aigrain S., Mazeh T., 2013, *MNRAS*, **432**, 1203
- McQuillan A., Mazeh T., Aigrain S., 2014, *ApJS*, **211**, 24
- Mermilliod J.-C., Mermilliod M., Hauck B., 1997, *A&AS*, **124**, 349
- Michaud G., 1970, *ApJ*, **160**, 641
- Michaud G., Charland Y., Megessier C., 1981, *A&A*, **103**, 244
- Montgomery M. H., O'Donoghue D., 1999, *Delta Scuti Star Newsletter*, **13**, 28
- Munteanu C., Negrea C., Echim M., Mursula K., 2016, *Annales Geophysicae*, **34**, 437
- Murphy S. J., Hey D., Van Reeth T., Bedding T. R., 2019, *MNRAS*, **485**, 2380
- Neiner C., Lampens P., 2015, *MNRAS*, **454**, L86
- Neiner C., Wade G. A., Sikora J., 2017, *MNRAS*, **468**, L46
- O'Leary R. M., Burkart J., 2014, *MNRAS*, **440**, 3036
- Pamyatnykh A. A., 2000, in Breger M., Montgomery M., eds, *Astronomical Society of the Pacific Conference Series Vol. 210, Delta Scuti and Related Stars*. p. 215 ([arXiv:astro-ph/0005276](https://arxiv.org/abs/astro-ph/0005276))
- Panchuk V. E., Chuntunov G. A., Naidenov I. D., 2014, *Astrophysical Bulletin*, **69**, 339
- Panchuk V. E., Klochkova V. G., Yushkin M. V., 2017, *Astronomy Reports*, **61**, 820
- Paunzen E., Wraight K. T., Fossati L., Netopil M., White G. J., Bewsher D., 2013, *MNRAS*, **429**, 119
- Petit P., et al., 2011, *A&A*, **532**, L13
- Preston G. W., 1974, *ARA&A*, **12**, 257
- Prša A., Zwitter T., 2005, *ApJ*, **628**, 426
- Raskin G., et al., 2011, *A&A*, **526**, A69
- Rebeiro E., 1966, *POHP*, **8**, 24
- Sagar R., et al., 2011, *Current Science*, **101**, 1020
- Sanford R. F., 1931, *ApJ*, **74**, 201
- Santos A. R. G., Cunha M. S., Avelino P. P., García R. A., Mathur S., 2017, *A&A*, **599**, A1
- Santos A. R. G., García R. A., Mathur S., Bugnet L., van Saders J. L., Metcalfe T. S., Simonian G. V. A., Pinsonneault M. H., 2019, *ApJS*, **244**, 21
- Santos A. R. G., Mathur S., García R. A., Cunha M. S., Avelino P. P., 2021, *MNRAS*
- Savanov I. S., 2018, *Astronomy Reports*, **62**, 814
- Savanov I. S., Strassmeier K. G., 2008, *Astronomische Nachrichten*, **329**, 364
- Scargle J. D., 1989, in *Bulletin of the American Astronomical Society*. p. 1069
- Sinhal S. D., Kandpal C. D., Mahra H. S., Joshi S. C., Srivastava J. B., 1972, in *Optical astronomy with moderate size telescopes*. pp 20–34
- Slettebak A., 1986, *PASP*, **98**, 867
- Smalley B., et al., 2017, *MNRAS*, **465**, 2662
- Smith J. C., et al., 2012, *PASP*, **124**, 1000
- Snedden C., Bean J., Ivans I., Lucatello S., Sobek J., 2012, *MOOG: LTE line analysis and spectrum synthesis*, *Astrophysics Source Code Library* (ascl:1202.009)
- Sriram S., et al., 2018, in *Proc. SPIE*. p. 107026K, [doi:10.1117/12.2313165](https://doi.org/10.1117/12.2313165)
- Stumpe M. C., et al., 2012, *PASP*, **124**, 985
- Thompson S. E., et al., 2012, *ApJ*, **753**, 86
- Torrence C., Compo G. P., 1998, *Bulletin of the American Meteorological Society*, **79**, 61
- Trust O., Jurua E., De Cat P., Joshi S., 2020, *MNRAS*, **492**, 3143
- Trust O., Jurua E., De Cat P., Joshi S., Lampens P., 2021, *MNRAS*, **504**, 5528
- VanderPlas J. T., 2018, *ApJS*, **236**, 16
- Welsh B. Y., Montgomery S., 2013, *PASP*, **125**, 759
- Welsh W. F., et al., 2011, *ApJS*, **197**, 4
- Wheeler A., Kipping D., 2019, *MNRAS*, **485**, 5498
- White T. R., et al., 2017, *MNRAS*, **471**, 2882
- van Kooten M. A. M., Kenworthy M., Doelman N., 2020, *MNRAS*, **499**, 2817

APPENDIX A: AUTHOR AFFILIATIONS

- ¹Aryabhata Research Institute of Observational Sciences, Manora Peak, Nainital-263002, India
- ²Department of Physics, Mbarara University of Science and Technology, P.O. Box 1410, Mbarara, Uganda
- ³National Astronomical Research Institute of Thailand, Chiangmai 50180, Thailand
- ⁴Special Astrophysical Observatory, Russian Academy of Sciences, Nizhnii Arkhyz 369167, Russia
- ⁵Affiliate Faculty, Physics and Astronomy Department, George Mason University, Fairfax, VA 22030, USA
- ⁶Royal Observatory of Belgium, Ringlaan 3, B-1180 Brussel, Belgium
- ⁷Jeremiah Horrocks Institute, University of Central Lancashire, Preston PR1 2HE, UK
- ⁸CEA, Université Paris-Saclay, F-91191 Gif-sur-Yvette, France
- ⁹AIM, CEA, CNRS, Université Paris-Saclay, Université Paris Diderot, Sorbonne Paris Cité, F-91191 Gif-sur-Yvette, France
- ¹⁰Universidad de La Laguna (ULL), Departamento de Astrofísica, E-38206 La Laguna, Tenerife, Spain
- ¹¹Instituto de Astrofísica de Canarias (IAC), E-38205 La Laguna, Tenerife, Spain
- ¹²Department of Physics, University of Warwick, Coventry, CV4 7AL, UK
- ¹³Space Science Institute, 4765 Walnut Street, Suite B, Boulder, CO 80301, USA
- ¹⁴Indian Institute of Astrophysics, Koramangala, Bangalore-560034, India
- ¹⁵Department of Physics, University of Texas at Arlington, Arlington, TX 76019, USA
- ¹⁶Department of Physics and Astronomy, National Institute of Technology, Rourkela - 769008, Odisha, India
- ¹⁷Copernicus Astronomical Center, Bartycka 18, PL-00-716 Warsaw, Poland
- ¹⁸Çanakkale Onsekiz Mart University, Faculty of Sciences and Arts, Physics Department, 17100 Canakkale, Turkey
- ¹⁹Centre for Space Research, North-West University, South Africa
- ²⁰Stellar Astrophysics Centre, Department of Physics and Astronomy, Aarhus University, Ny Munkegade 120, Denmark
- ²¹Institute of Astronomy, Russian Academy of Sciences, Moscow-119017, Russia

²²Institut d’Astronomie et d’Astrophysique, Université Libre de Bruxelles, Boulevard du Triomphe, 1050-Bruxelles, Belgium

²³Kourovka Astronomical Observatory, Ural Federal University, Yekaterinburg, Russia

²⁴M. V. Lomonosov Moscow State University, P. K. Shternberg State Astronomical Institute, Moscow, Russia

²⁵SoS in Physics and Astrophysics, Pt. R. S. University, Raipur-492010, India

²⁶Institute of Informatics and Communication, University of Delhi South Campus, New Delhi, India

²⁷Department of Physics, Kyambogo University, P. O. Box 1, Kyambogo, Kampala, Uganda

²⁸Indian Institute of Science (IISc), Bengaluru, India

APPENDIX B: K2 PHOTOMETRIC DATA ANALYSIS

We analysed the K2 data discussed in Section 2.2. From these data sets, the flux (in $\text{e}^- \text{s}^{-1}$), F_i , over a set of N sample times, t_i , with indices $i = \{0, 1, 2, \dots, N-1\}$, was analysed to search for photometric variability. The analysis processes, as described below, were applied to the long cadence data of all stars. The analysis of the short cadence data acquired for HD 73045 was performed in a similar manner.

To begin, each time step, t_i , was defined in a way that $t_0 = 0$; this was done by subtracting the original Barycentric Julian Date (BJD) times, τ_i , by that of the first point, τ_0 , using

$$t_i = \tau_i - \tau_0, \quad (\text{B1})$$

where $\tau_0 = 2\,457\,139.63$ days, $2\,458\,095.49$ days, and $2\,458\,251.57$ days for C05, C16, and C18, respectively.

The flux data were re-calibrated as a magnitude deviation, Δm_i , of each flux, F_i , from its mean, $\langle F \rangle$. For all N data points in a data set, at a corresponding time, t_i , the i -th magnitude deviation data point in the series is defined by

$$\Delta m_i = -2500 \log_{10} \left(\frac{F_i}{\langle F \rangle} \right), \quad (\text{B2})$$

where Δm_i is calculated in mmag (hence the incorporated factor of 1000). To prepare these data for the signal analysis process, variable artifacts, such as those possibly left over from the PDC process were removed by subtracting an eighth order polynomial, although it is noted that such artifact removal may also cancel any intrinsic variability component of a corresponding frequency. Subsequently, the signal search was focused on periods shorter than 20 days. The median value of the data was also subtracted. As an example, the analysed photometric light curve of HD 73045 obtained during C18 campaign is shown in Fig. 3 (top-left, blue points).

To analyse a light curve in the frequency domain, the Lomb-Scargle (LS) algorithm (Lomb 1976; Scargle 1989) was applied to the time-series data, noting that the original SAP data are irregularly sampled. The Nyquist frequency $(2dt)^{-1}$ for LC (29.4 min cadence) and SC (58.8 s cadence) sampling are $\sim 24.5 \text{ d}^{-1}$ and $\sim 735 \text{ d}^{-1}$, respectively. Each campaign occupies its own temporal range T , giving in a respective frequency resolution, Δf . For example, C18 has a temporal window of $T = 50.814 \text{ d}$, providing a frequency resolution of $\Delta f = 0.0197 \text{ d}^{-1}$ that allows an estimate for the peak frequencies and corresponding amplitudes. To improve signal peak definition and to better estimate the peak frequencies and amplitudes, oversampling was applied to provide a frequency domain sampled every 0.001 d^{-1} .

Although the half-width at half-maximum (HWHM) of a peak is often used to estimate the accuracy of the peak frequency, VanderPlas (2018) suggests avoiding this approach through computing the false-alarm probability (FAP) for each peak. This criterion estimates the probability that a peak was produced by noise as opposed to an inherent signal. The lower the value of the FAP, the more likely that a given peak is real. Furthermore, Frescura et al. (2008) noted the subjectivity of the noise level determination in calculating the signal-to-noise ratio, which is often used to select relevant peaks from the background noise spectrum (Breger et al. 1993). Therefore, while the amplitude signal-to-noise value was calculated for candidate signal peaks, through the use of a smoothing function across the frequency spectrum to calculate the noise spectrum, the FAP was used as the selection criterion to determine a signal’s validity. For this study, the independent frequency method (VanderPlas 2018) was applied to calculate the FAPs of respective spectral amplitudes across the frequency domain. After a provisional analysis, a threshold FAP of 10^{-8} was adopted across all data sets to provide a consistent, conservative criterion for identifying true signals amongst the noise, which is noted by Bowman et al. (2018) to be particularly significant at low frequencies. An example periodogram (logarithm of the period versus amplitude) is shown in Fig. 3 (bottom, blue-line) for the C18 data set for HD 73045. The frequencies, periods, and amplitudes for peaks with FAP values of 10^{-8} and below, for all stars during their respective campaigns as a result of performing the Lomb-Scargle analysis are listed in Table B1.

Next, the time-series data were analysed to determine the frequency, f , amplitude, A , and the phase at $t_0 = 0$, $\phi(t_0)$, from which a model of the light curve was constructed. Using the results of the Lomb-Scargle analysis as initial starting points, sinusoidal components incorporating these parameters were determined by sequentially fitting a series of components in the form of a sinusoid plus an offset, Z , to the data:

$$\Delta m_i = Z + A \sin(2\pi f t_i + \phi), \quad (\text{B3})$$

where ϕ is the phase derived from the fit and is described below.

Using the methods of Montgomery & O’Donoghue (1999), the corresponding errors, $\sigma(f)$, $\sigma(A)$, and $\sigma(\phi)$, were also derived using:

$$\sigma(f) = \sqrt{\frac{6}{N}} \frac{1}{\pi \mathcal{T}} \frac{\sigma(\Delta m)}{A}, \quad (\text{B4})$$

$$\sigma(A) = \sqrt{\frac{2}{N}} \sigma(\Delta m), \quad (\text{B5})$$

$$\sigma(\phi) = \sqrt{\frac{2}{N}} \frac{\sigma(\Delta m)}{A}. \quad (\text{B6})$$

Here, N is the number of terms in a regularly sampled time series with an interval Δt , $\mathcal{T} = N\Delta t$ is the time range of the data set, A is the amplitude of the sinusoidal fit, and $\sigma(\Delta m)$ is the root mean square of the flux deviation values.

To determine these sinusoidal parameters and their uncertainties, the data were resampled at the regular 29.4-min cadence using cubic spline interpolation. Next, the time was adjusted such that the zero point was placed at the center of the data set by subtracting the average of the resampled time array. Using the Lomb-Scargle results as a starting point, single sinusoids were sequentially fit using Eqn. B3 and subtracted from the time-series, until all components (i.e., those with

Lomb-Scargle FAP values below the threshold) were accounted for. The fitting process allowed the amplitude to vary within 20 per cent about its LS value, while the frequency was allowed to vary within 0.01 d^{-1} about its input value. From the resulting phase value, ϕ , which is determined at this central point, the phase of the first point of the fit, $\phi(t_0)$, was calculated.

For any component with a variation period P , the phase of each data point ϕ_i , at time t_i relative to the first point in the data series at time t_0 , can be calculated using

$$\phi_i = 2\pi \left(\frac{t_i - t_0}{P} - \left\lfloor \frac{t_i - t_0}{P} \right\rfloor \right), \quad (\text{B7})$$

which simplifies when $t_0 = 0$. From this, phase-folded plots of the time-series were produced corresponding to the dominant period of each star for each campaign. The C18 HD 73045 data are folded to the dominant period of 12.64 d in Fig. 3 (top-right) along with a sinusoidal fit to this component (red-line) with the parameters given in Table 3.

Table B1. Flux variation signal properties (ordered by amplitude) derived from applying the Lomb-Scargle analysis to the all flux-deviation data sets. For HD 73045, C18, refer to the blue-line peaks of Fig. 3 (bottom).

Star Name	Campaign	Frequency (d^{-1})	Period (d)	Amplitude (mmag)	$\log_{10}(\text{FAP})$
HD 73045	C05	0.078	12.82	0.112	-302
		0.155	6.452	0.039	-33
		0.054	18.52	0.0309	-18
		0.138	7.246	0.029	-17
		0.171	5.848	0.022	-8
	C18	0.079	12.66	0.039	-95
		0.155	6.452	0.022	-29
HD 76310	C05	0.217	4.608	0.498	-361
		0.186	5.376	0.189	-49
		0.421	2.375	0.113	-15
		0.049	20.41	0.105	-13
		0.159	6.289	0.095	-10
	C16	0.209	4.785	0.398	-331
		0.187	5.348	0.333	-231
		0.076	13.16	0.104	-19
		0.430	2.326	0.089	-13
		0.969	1.031	0.081	-11
		0.058	17.24	0.072	-8
		0.206	4.854	1.094	-420
	C18	0.177	5.650	0.275	-24
		0.430	2.326	0.188	-9
HD 73574	C05	0.070	14.29	0.8139	-76
		0.091	10.99	0.3827	-14
	C18	0.091	10.99	0.0513	-9
HD 73618	C05	0.264	3.788	0.415	-274
		0.205	4.878	0.228	-81
		0.410	2.439	0.152	-34
		0.244	4.098	0.104	-14
		0.431	2.320	0.102	-13
		0.184	5.435	0.086	-9
	C16	0.261	3.831	0.320	-254
		0.205	4.878	0.287	-203
		0.401	2.494	0.137	-44
		0.225	4.444	0.135	-43
		0.418	2.392	0.104	-24
		0.242	4.132	0.094	-19
		0.290	3.448	0.074	-10
		0.448	2.232	0.069	-9
	C18	0.266	3.759	0.595	-256
		0.213	4.695	0.249	-42
		0.196	5.102	0.194	-24
		0.417	2.398	0.190	-23
		0.238	4.202	0.125	-8
		0.295	3.390	0.123	-8
HD 73619	C05	0.077	12.987	0.388	-289
		0.155	6.452	0.210	-82
		0.233	4.292	0.160	-46
		0.058	17.241	0.108	-19
		0.042	20.810	0.098	-16
		0.310	3.226	0.095	-14
		0.096	10.417	0.082	-10
	C18	0.077	12.987	0.324	-217
		0.156	6.410	0.163	-52
		0.235	4.256	0.103	-19
		0.112	8.929	0.075	-9

APPENDIX C: SUPPLEMENTARY MATERIALS

This paper has been typeset from a \LaTeX file prepared by the author.

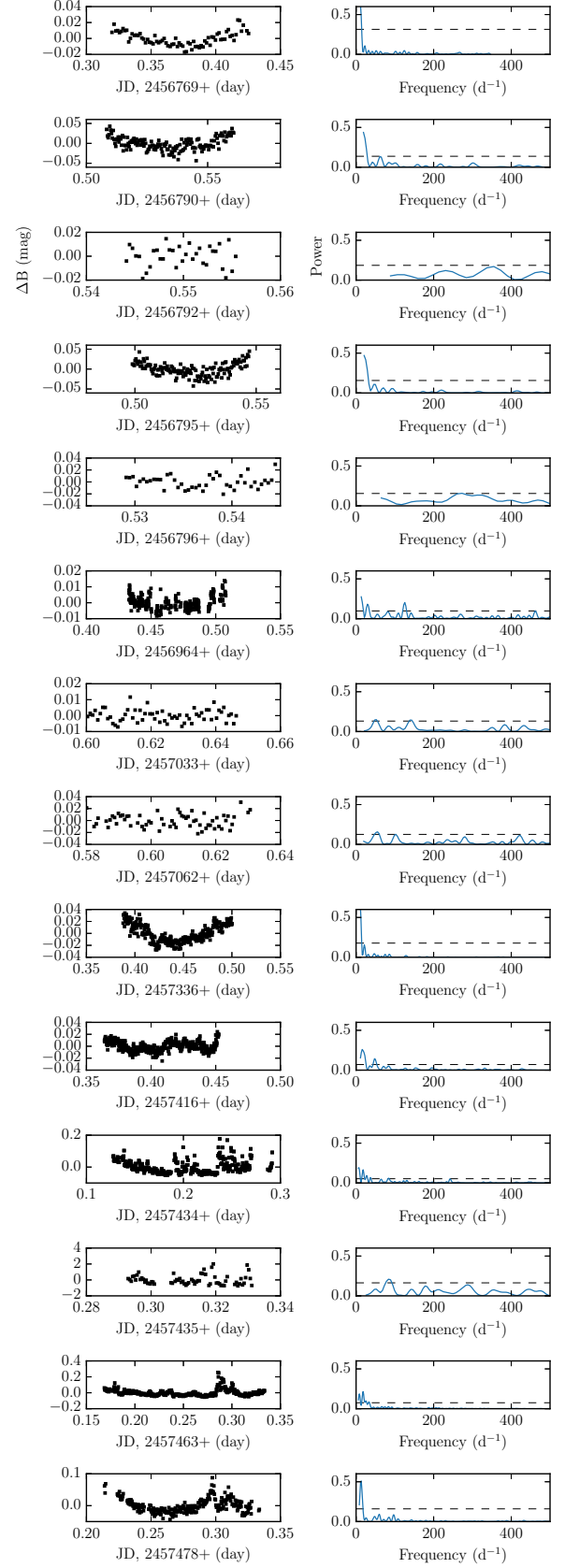


Figure C1. Light curves for HD 73045 from ground-based observations with B-filter.

Table C1. Ground-based CCD photometric observations of HD 73045 obtained from various optical telescopes located at different sites.

S. No.	Observatory	Telescope Diameter (m)	Filters	Exposure Time (s)	Total Durations (h)	Date dd-mm-yyyy	HJD (d)
1.	ARIES	1.04	V	2	1.47	16-04-2014	2456764
2.			V	3	0.92	20-04-2014	2456768
3.	Devasthal	1.30	B	5	2.53	21-04-2014	2456769
4.			B	5	1.80	02-11-2014	2456964
5.			V	4	1.47	11-11-2014	2456973
6.			B	4	0.17	30-11-2014	2456992
7.			V	15	0.85	30-12-2015	2457387
8.			V	10	0.57	27-01-2016	2457415
9.			B	15	2.12	28-01-2016	2457416
10.			V	3	2.02	19-12-2016	2457742
11.	MASTER-II -URAL	0.40	B, V	5	2.92, 2.92	09-11-2015	2457336
12.			B	5	1.35	22-01-2016	2457410
13.			B, V	5	0.13,0.13	13-02-2016	2457432*
14.			B	5	4.00	11-03-2016	2457459
15.			V	5	3.97	14-03-2016	2457463
16.			B, V	5	3.96, 3.96	15-03-2016	2457478
17.	PROMPT-8	0.60	B	4	1.26	12-05-2014	2456790
18.			B	4	0.27	14-05-2014	2456792
19.			B	4	1.65	16-05-2014	2456794
20.			B	15	1.10	11-01-2015	2457033
21.			B	20	1.21	09-02-2015	2457062

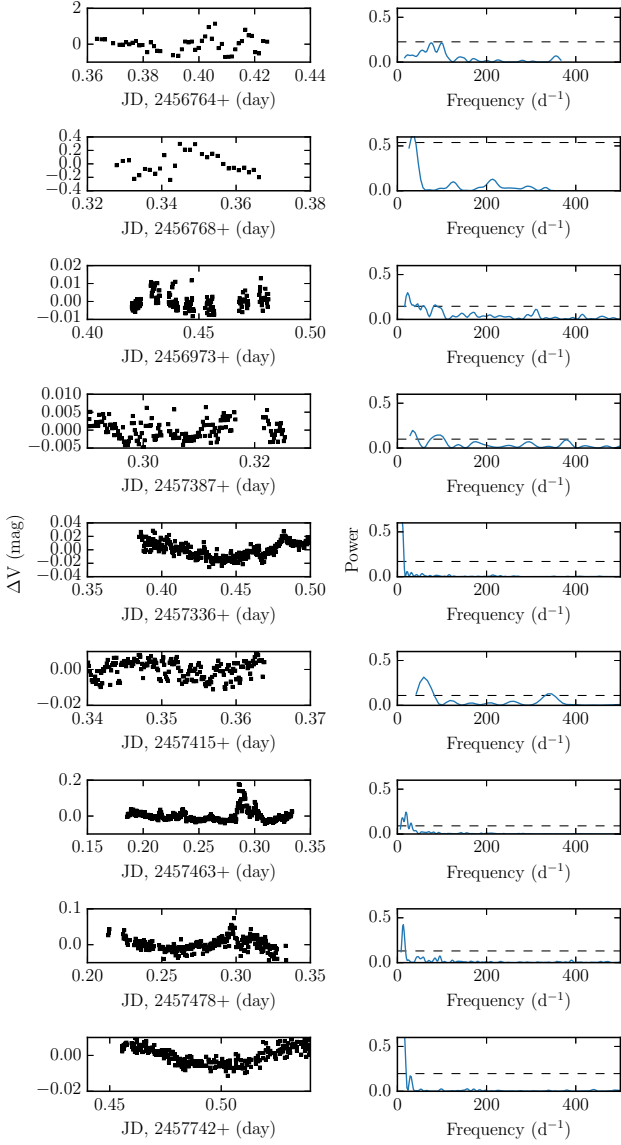


Figure C2. Light curves for HD 73045 from ground-observations with V-filter.

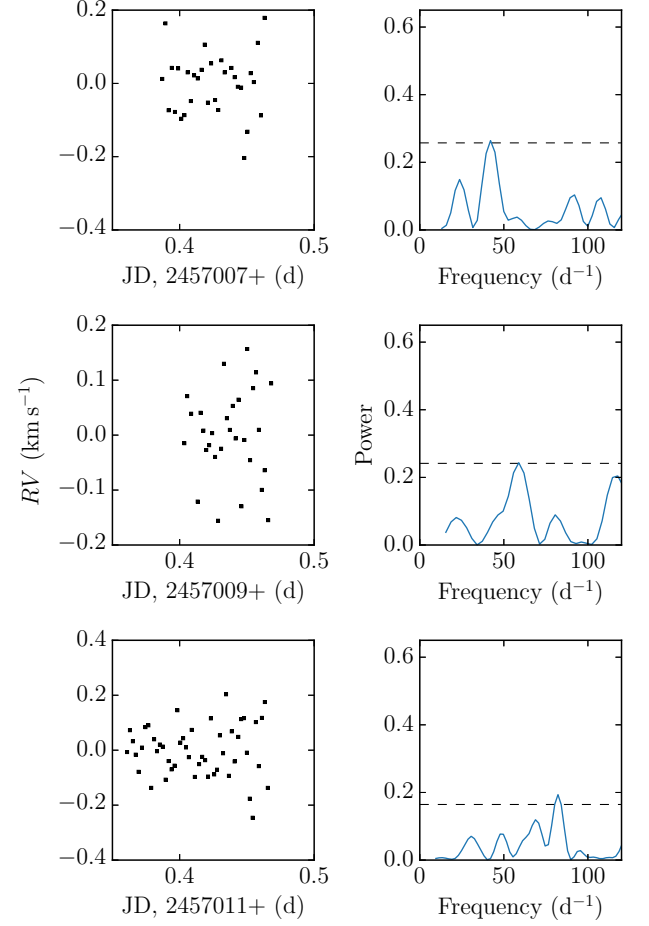


Figure C3. RV curve (panels on the left) and power spectrum (panels on the right) of the radial velocity measurements for HD 73045 from MRES data. The black horizontal dashed line in the power spectrum represents SNR of 4.

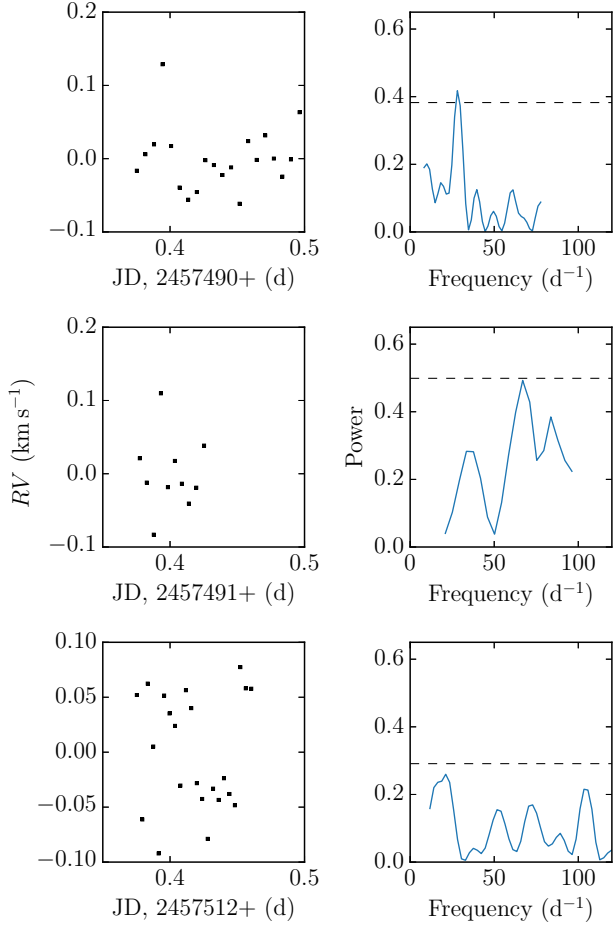


Figure C4. RV curve (*panels on the left*) and power spectrum (*panels on the right*) of the radial velocity measurements for HD 73045 from HERMES data. The black horizontal dashed line in the power spectrum represents SNR of 4.

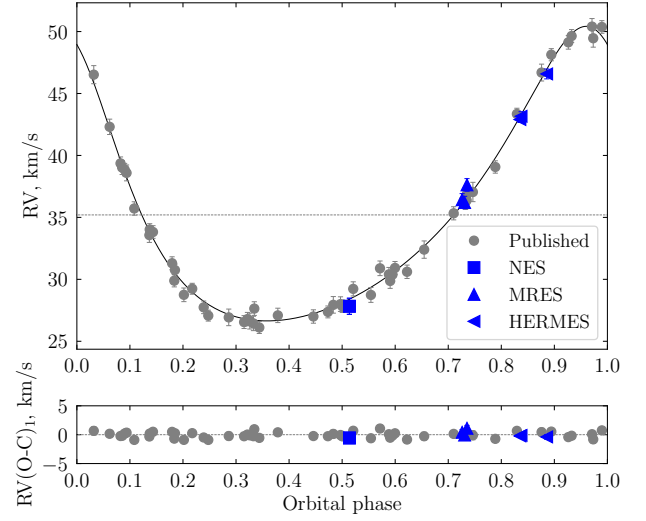


Figure C5. RV of HD 73045, as measured by us (blue), compared to the orbital solution by Carquillat & Prieur (2007) (grey).

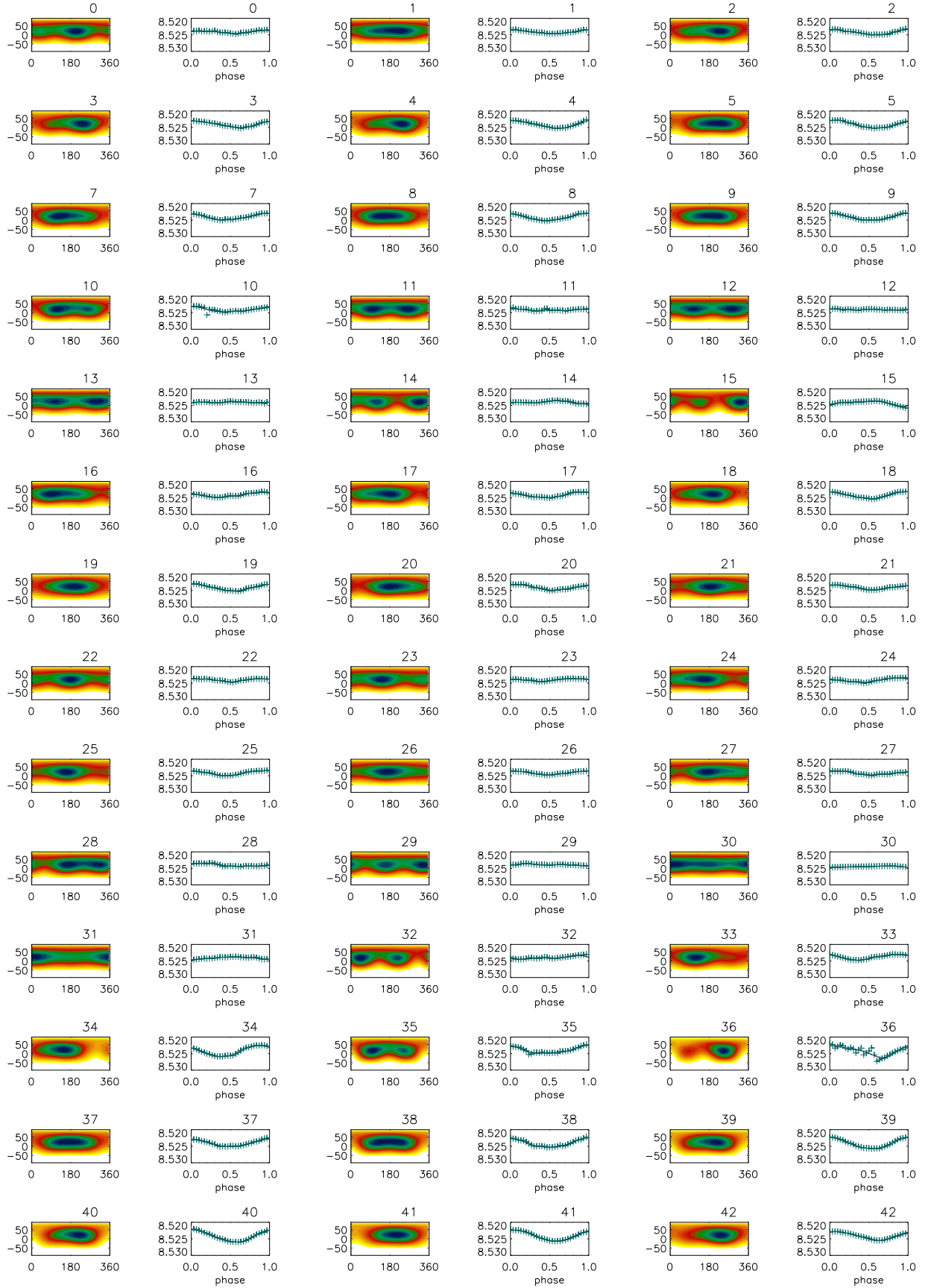


Figure C6. As Fig. 9, but spot maps for HD 76310.

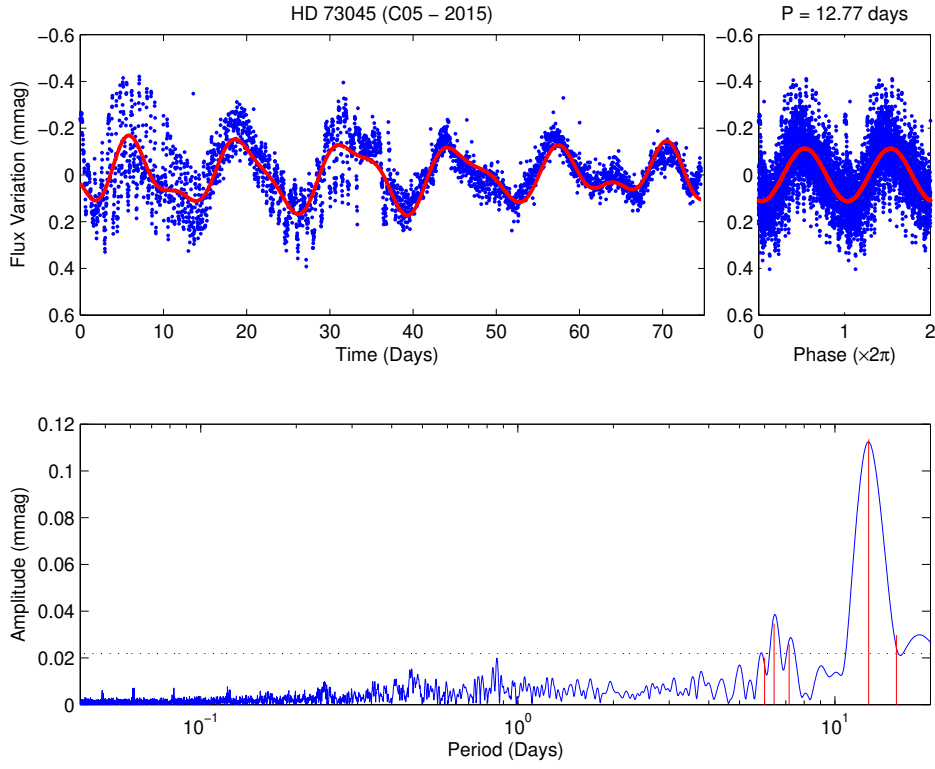


Figure C7. As Fig. 3, but for the LC K2 Campaign 5 observations of HD 73045.

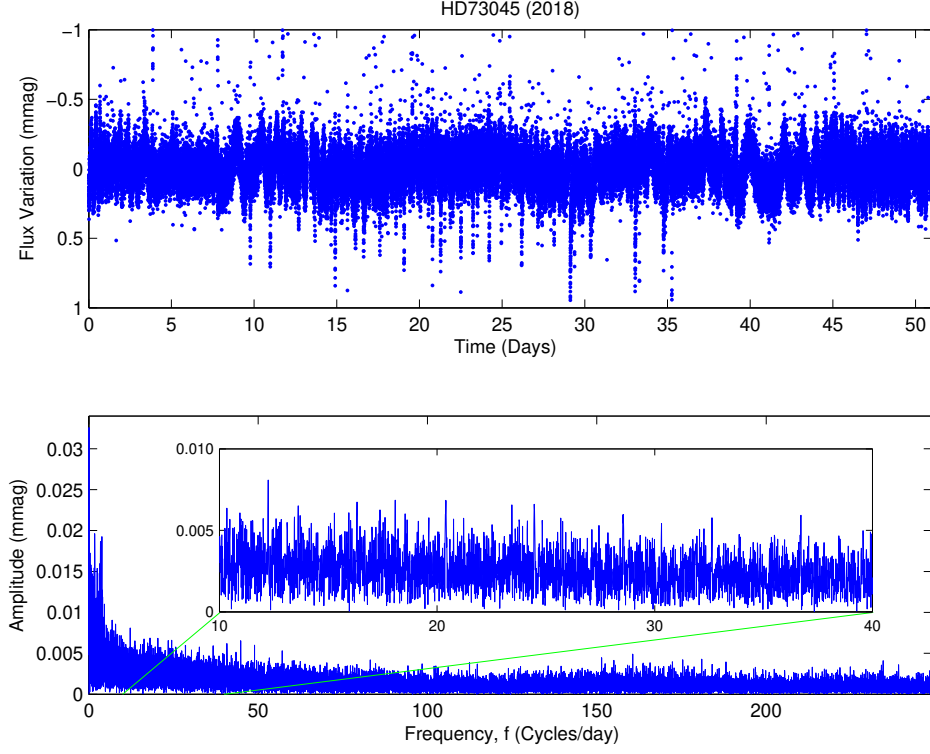


Figure C8. Top: Time series photometric variability (in mmag) of HD 73045 from the SC 2018 *K2* Campaign 18. The PDC_SAP data includes intrinsic signals as well as systemic and noise artifacts. Bottom: Frequency distribution of spectral amplitudes, in mmag, derived from applying the Lomb-Scargle algorithm to the time series. The frequency range from $10\text{--}40\text{ d}^{-1}$ is expanded into the inset to provide more detail of that range. It can be seen there are no signals related to those from the earlier ground-based observations and that this range is dominated by noise.

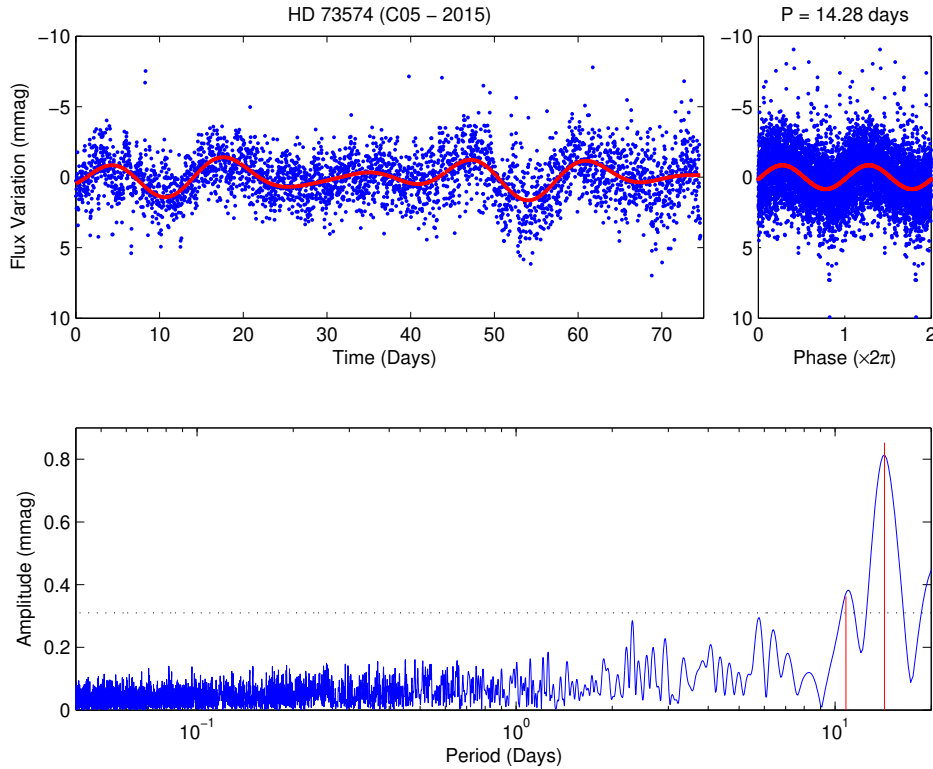


Figure C9. As Fig. 3, but for the LC *K2* Campaign 5 observations of HD 73754.

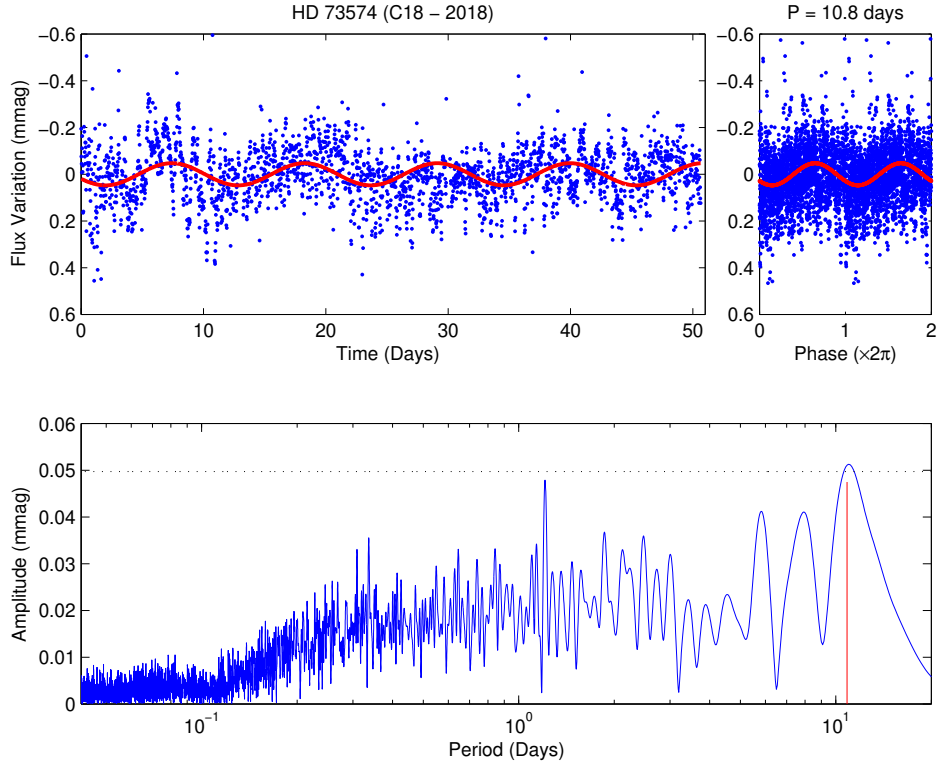


Figure C10. As Fig. 3, but for the LC K2 Campaign 18 observations of HD 73754.

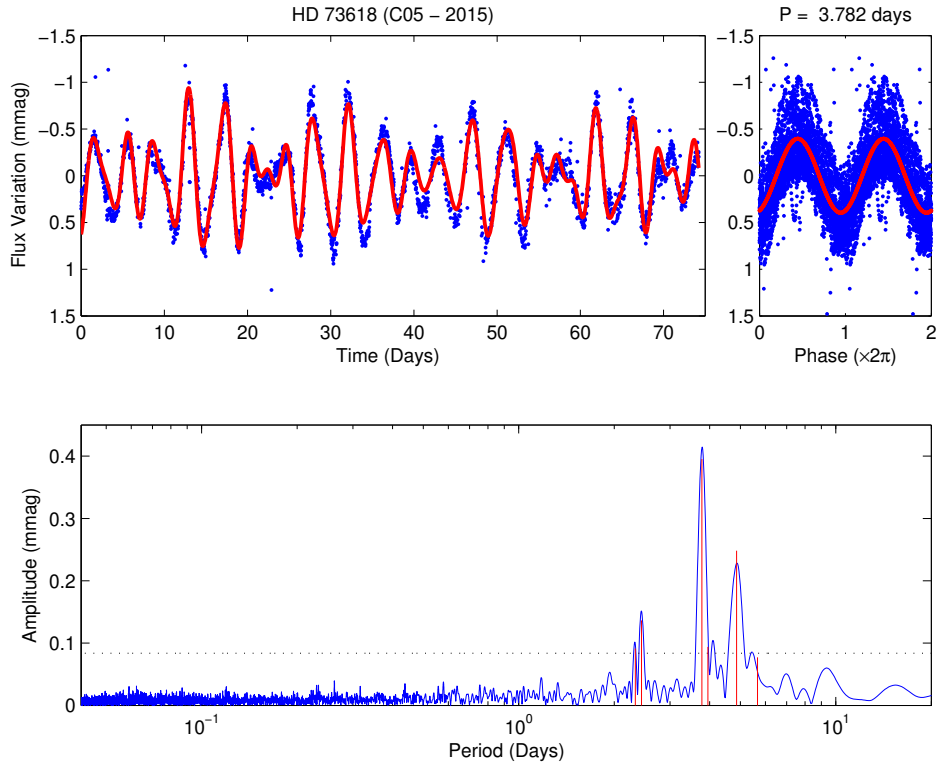


Figure C11. As Fig. 3, but for the LC K2 Campaign 5 observations of HD 73618.

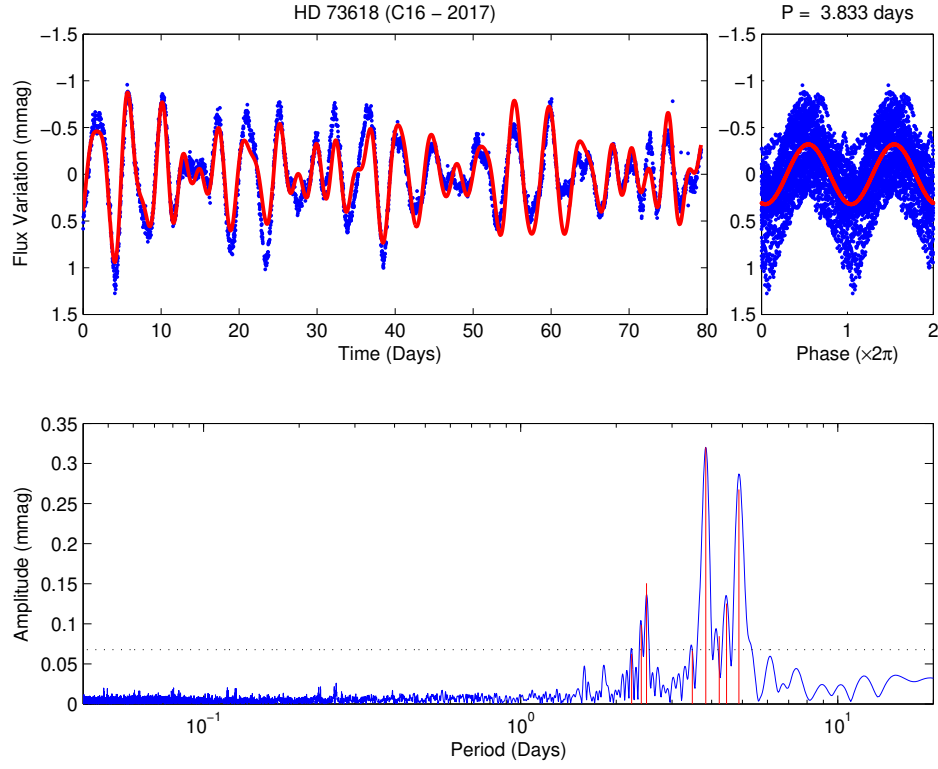


Figure C12. As Fig. 3, but for the LC K2 Campaign 16 observations of HD 73618.

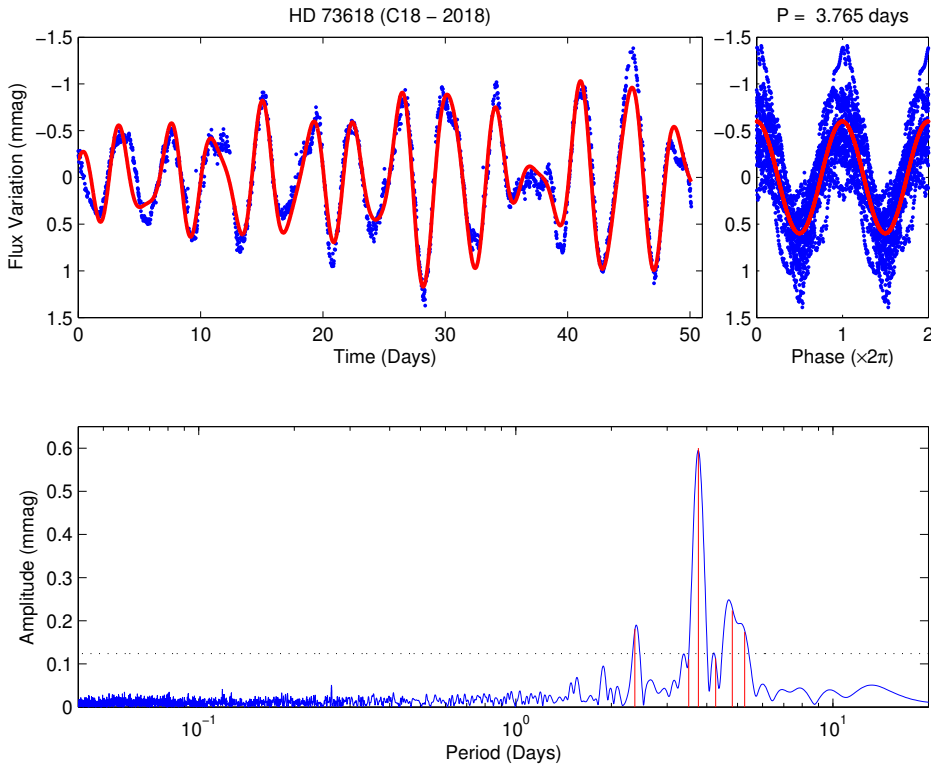


Figure C13. Time series (top) and respective Lomb-Scargle periodogram (bottom) for the LC K2 Campaign 18 observations of HD 73618.

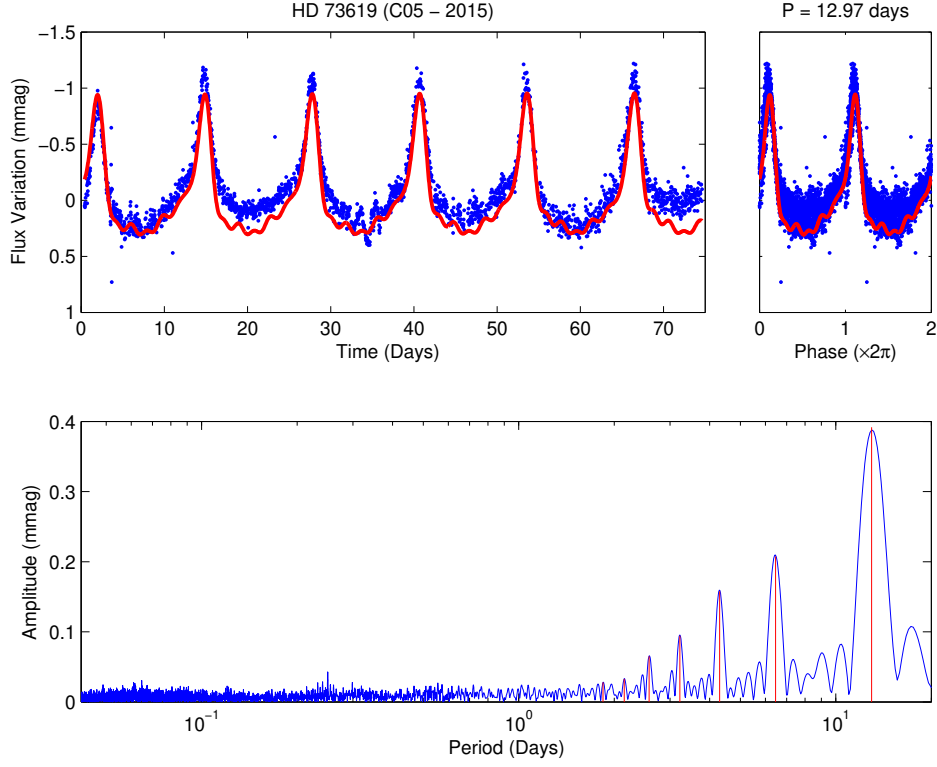


Figure C14. As Fig. 3, but for the LC K2 Campaign 5 observations of HD 73619. However, in contrast to the remainder of this paper, the phase diagram is traced by two periods of the light curve model, and not by the dominant component. Additionally, the FAP threshold criterion has been removed, with the model being constructed from the fundamental component and its overtones.

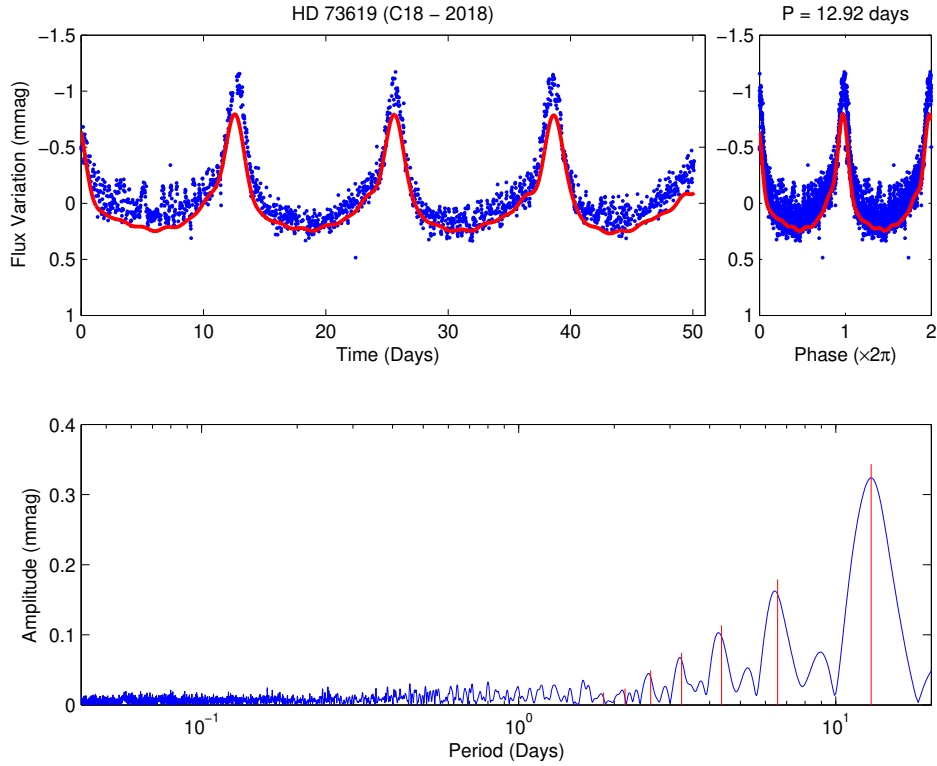


Figure C15. Time series (top) and respective Lomb-Scargle periodogram (bottom) for the LC K2 Campaign 18 observations of HD 73619.

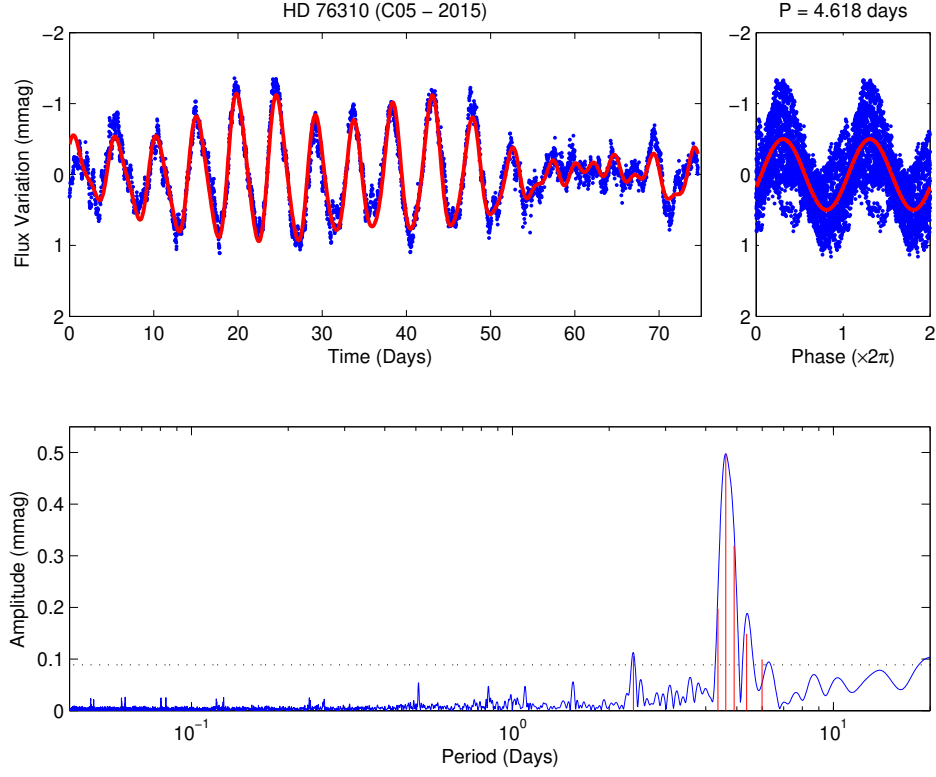


Figure C16. As Fig. 3, but for the LC K2 Campaign 5 observations of HD 76310.

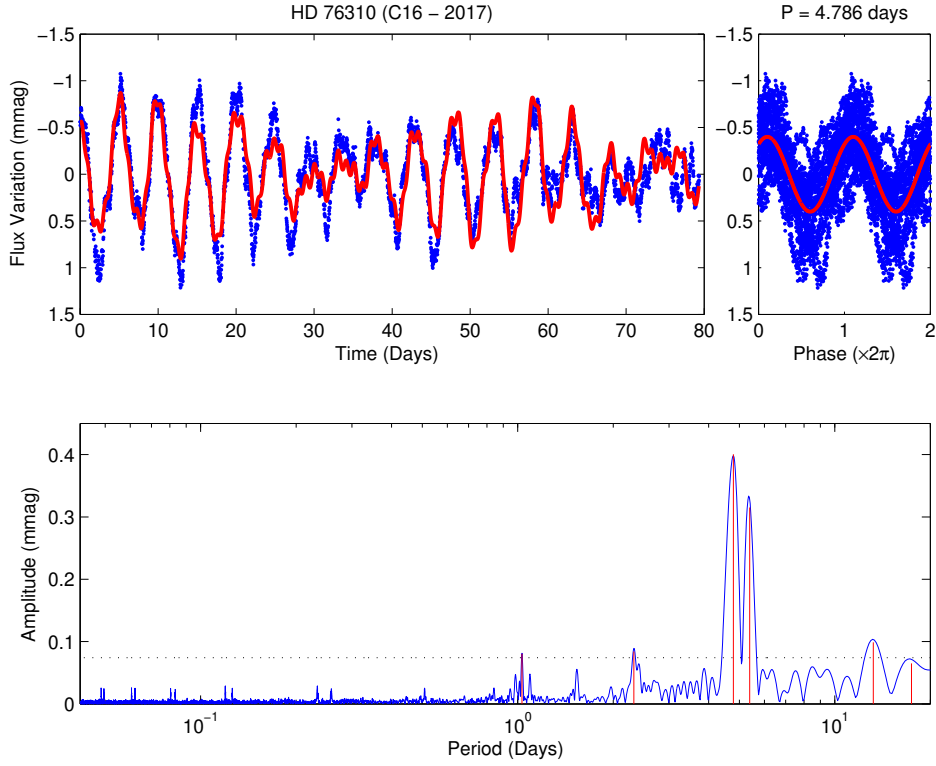


Figure C17. As Fig. 3, but for the LC K2 Campaign 16 observations of HD 76310.

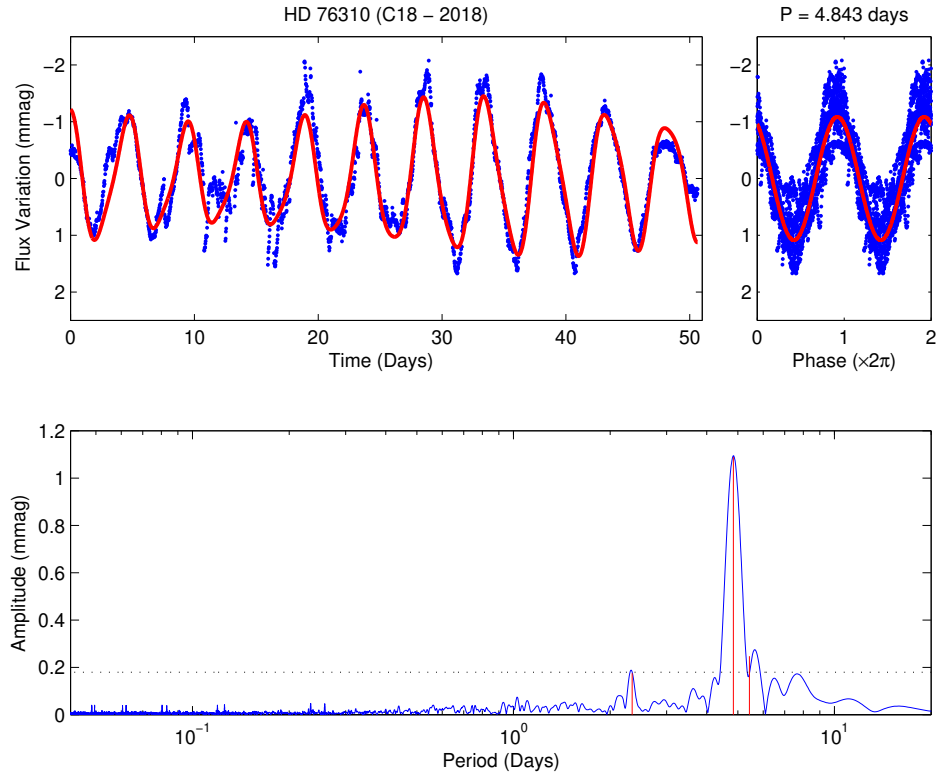


Figure C18. As Fig. 3, but for the LC *K2* Campaign 18 observations of HD 76310.

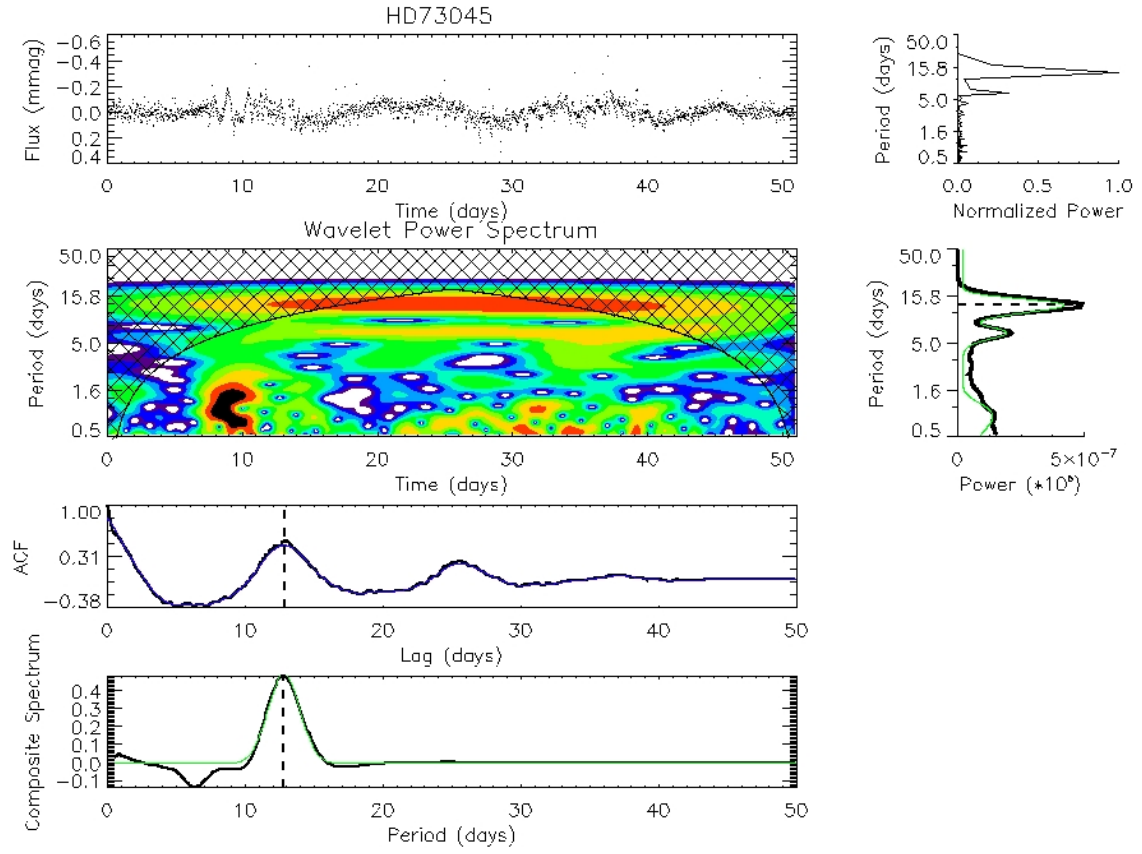


Figure C19. The wavelet map of HD 73045 based on K2 C18 data; see Fig. 10 for description details.

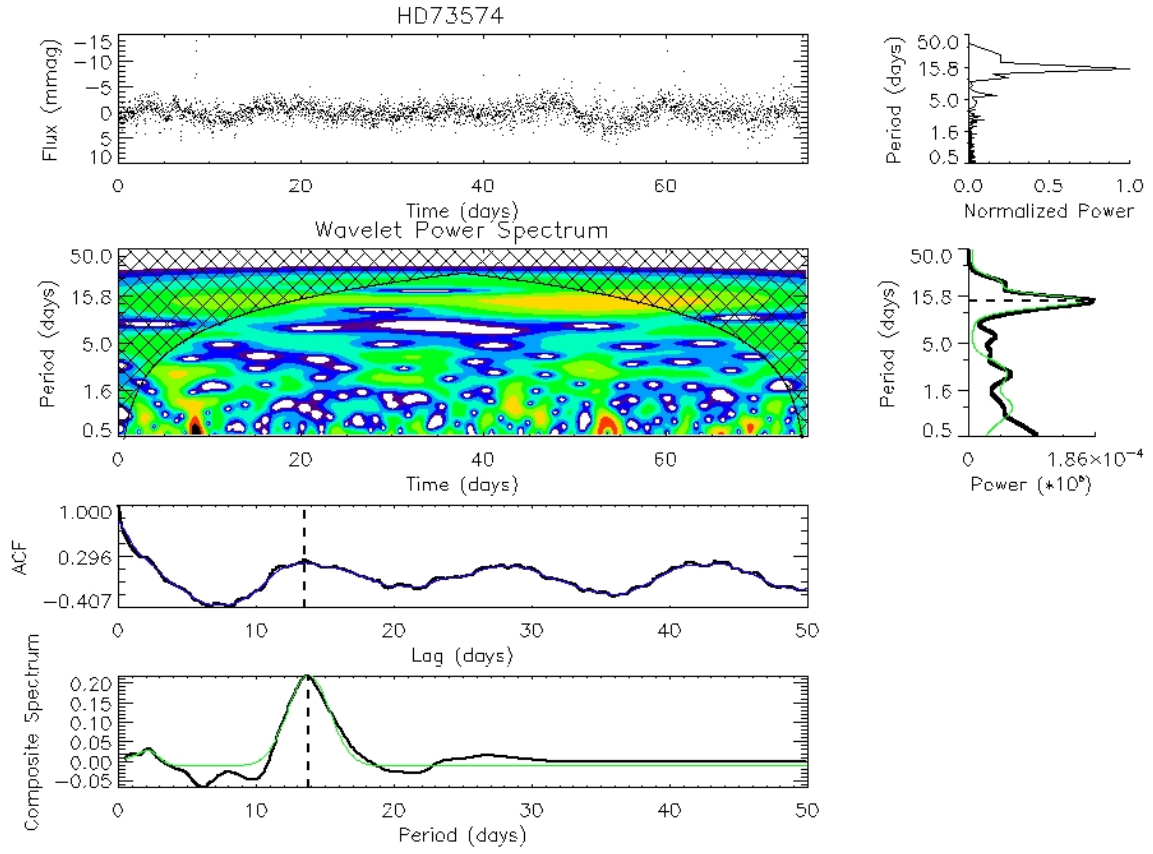


Figure C20. The wavelet map of HD 73574 based on C05 data. The description follows that for HD 73045, see Fig. 10.

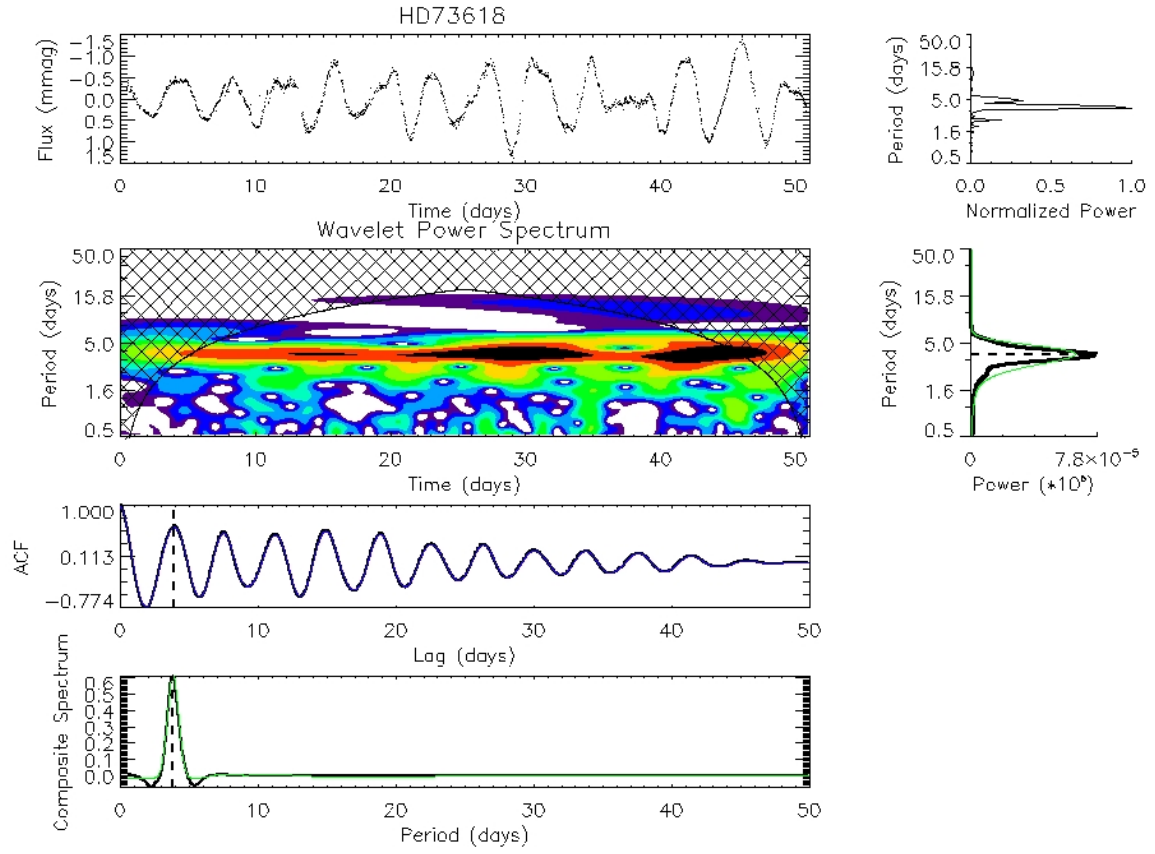


Figure C21. The wavelet map of HD 73618 based on C18 data. The description follows that for HD 73045, see Fig. 10.

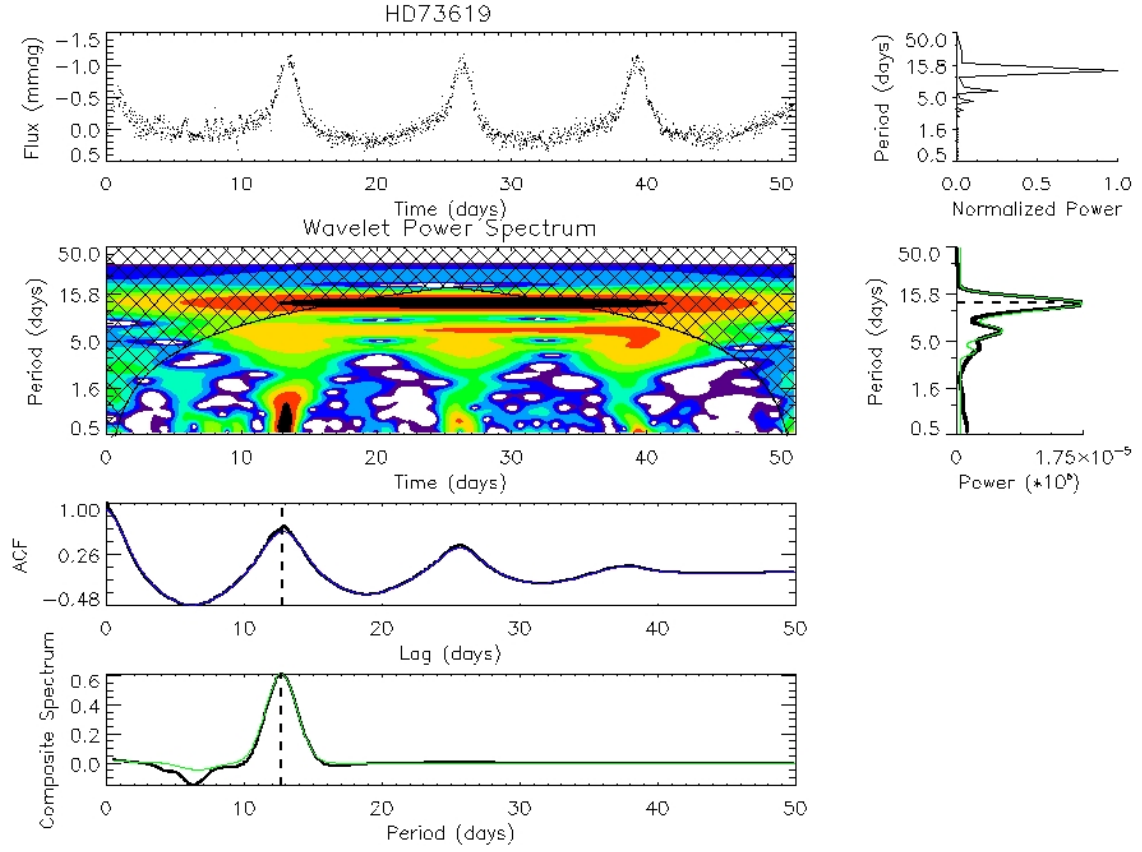


Figure C22. The wavelet map of HD 73619 based on C18 data. The description follows that for HD 73045, see Fig. 10.

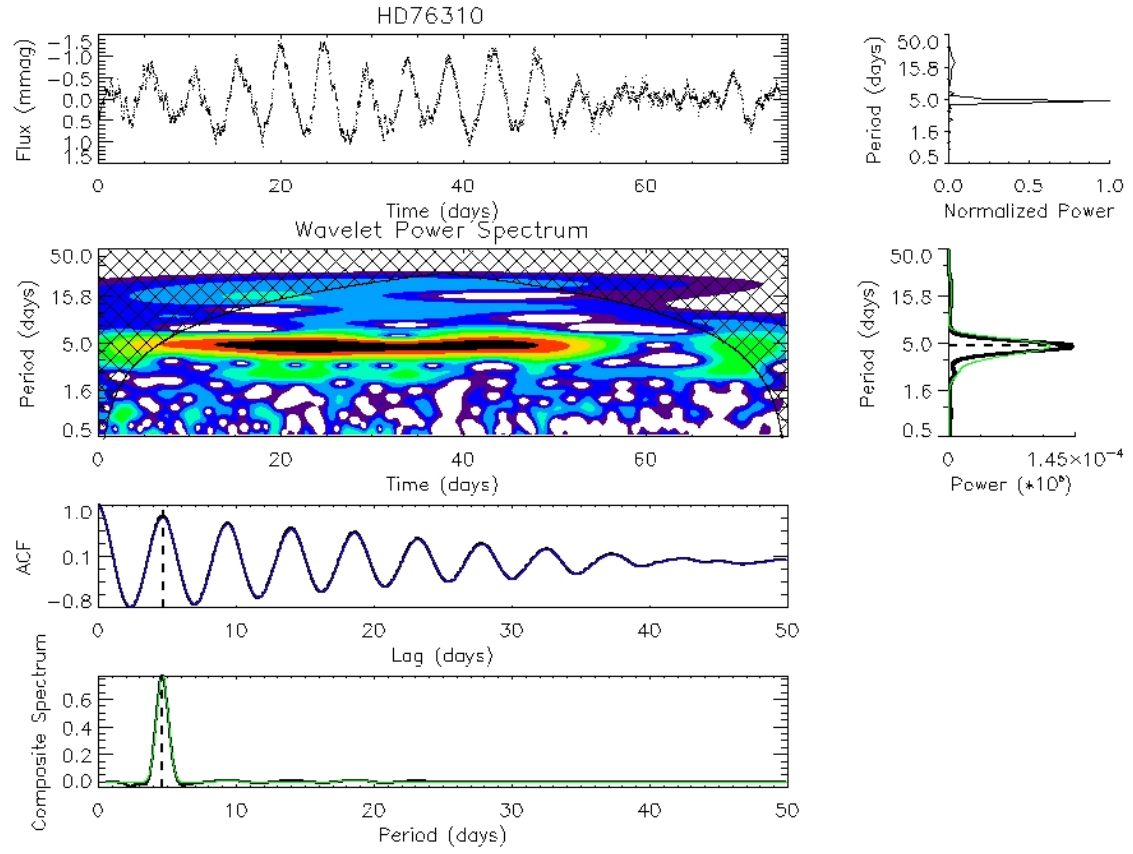


Figure C23. The wavelet map of HD 73610 based on C05 data. The description follows that for HD 73045, see Fig. 10.

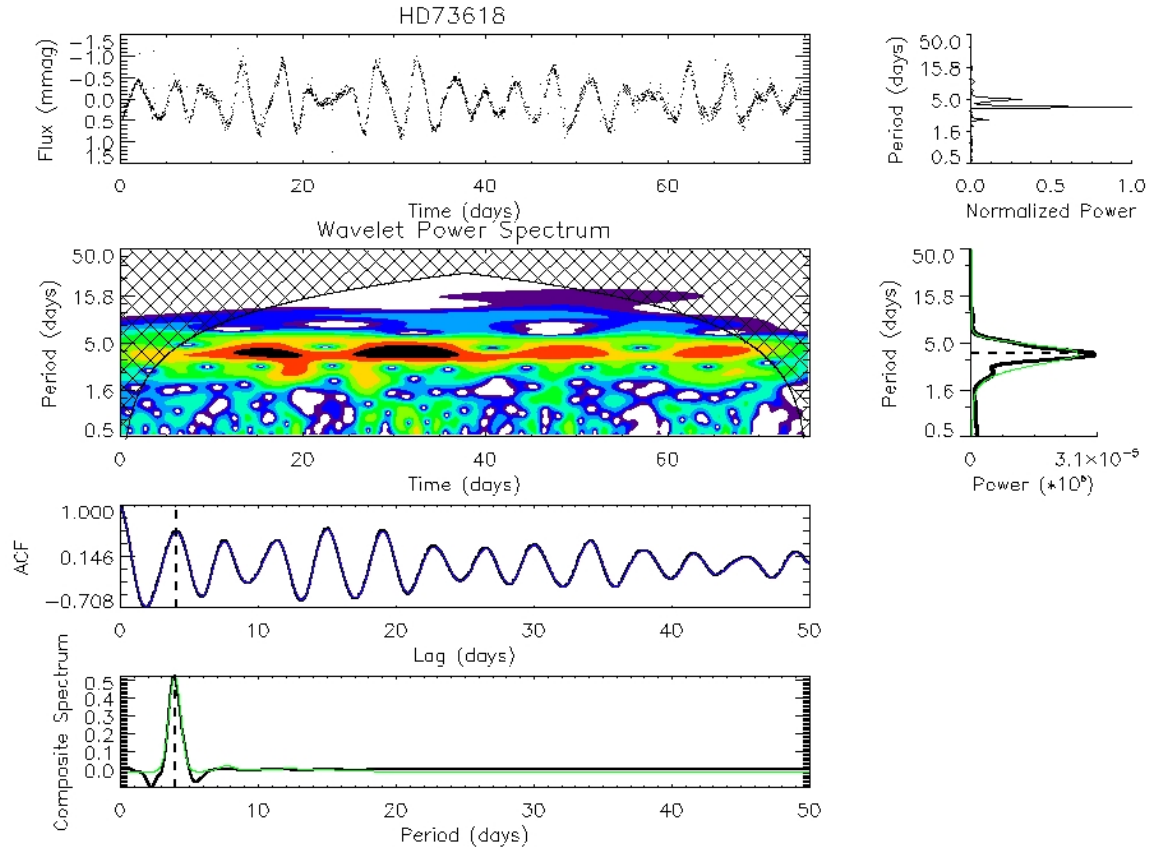


Figure C24. The wavelet map of HD 73618 based on K2 C05 data. The description follows that for HD 73045, see Fig. 10.

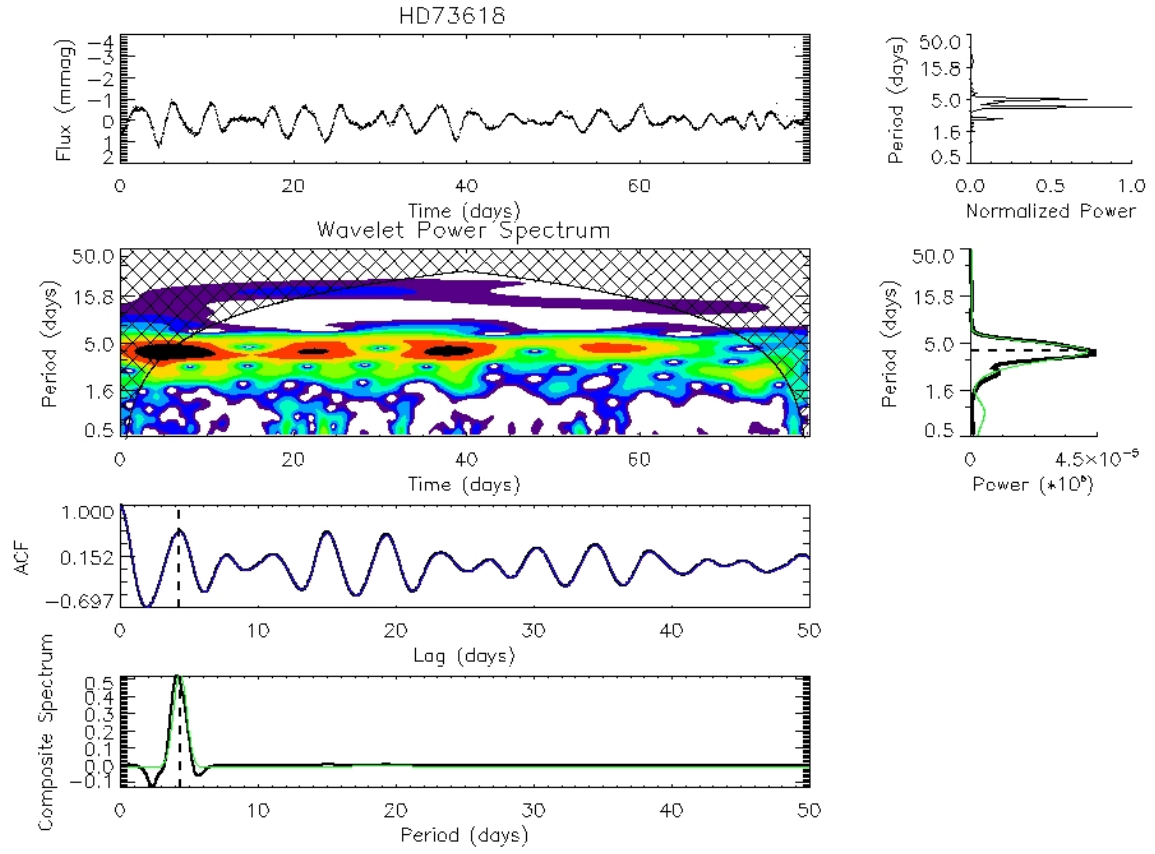


Figure C25. The wavelet map of HD 73618 based on K2 C16 data. The description follows that for HD 73045, see Fig. 10.

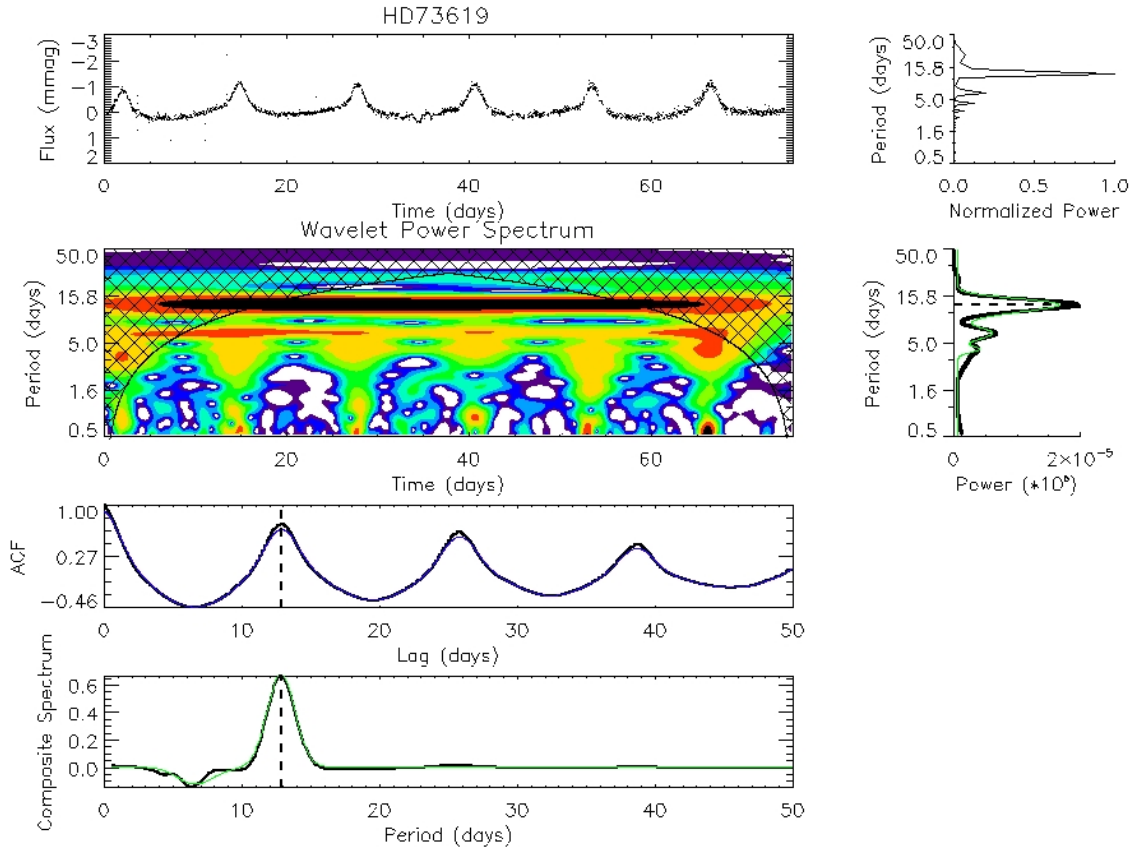


Figure C26. The wavelet map of HD 73619 based on K2 C05 data. The description follows that for HD 73045, see Fig. 10.

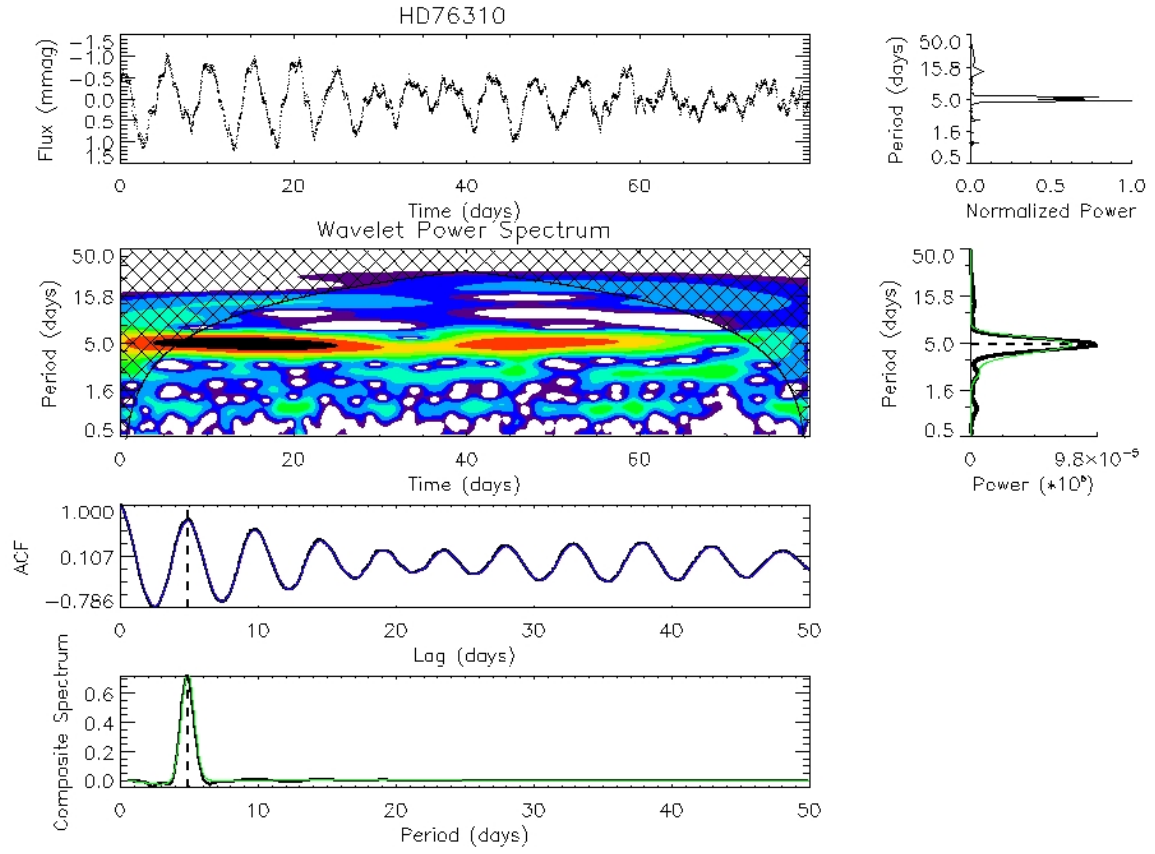


Figure C27. The wavelet map of HD 73610 based on K2 C16 data. The description follows that for HD 73045, see Fig. 10.

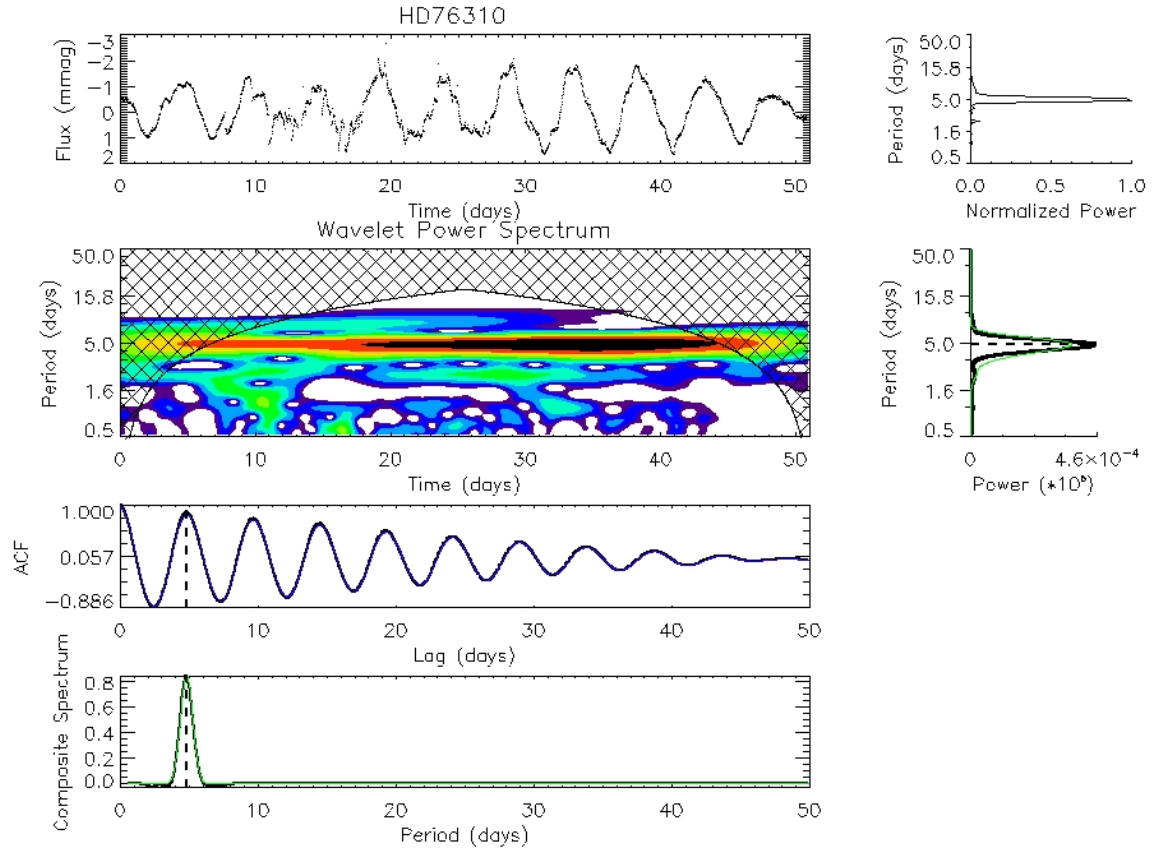


Figure C28. The wavelet map of HD 73610 based on K2 C18 data. The description follows that for HD 73045, see Fig. 10.

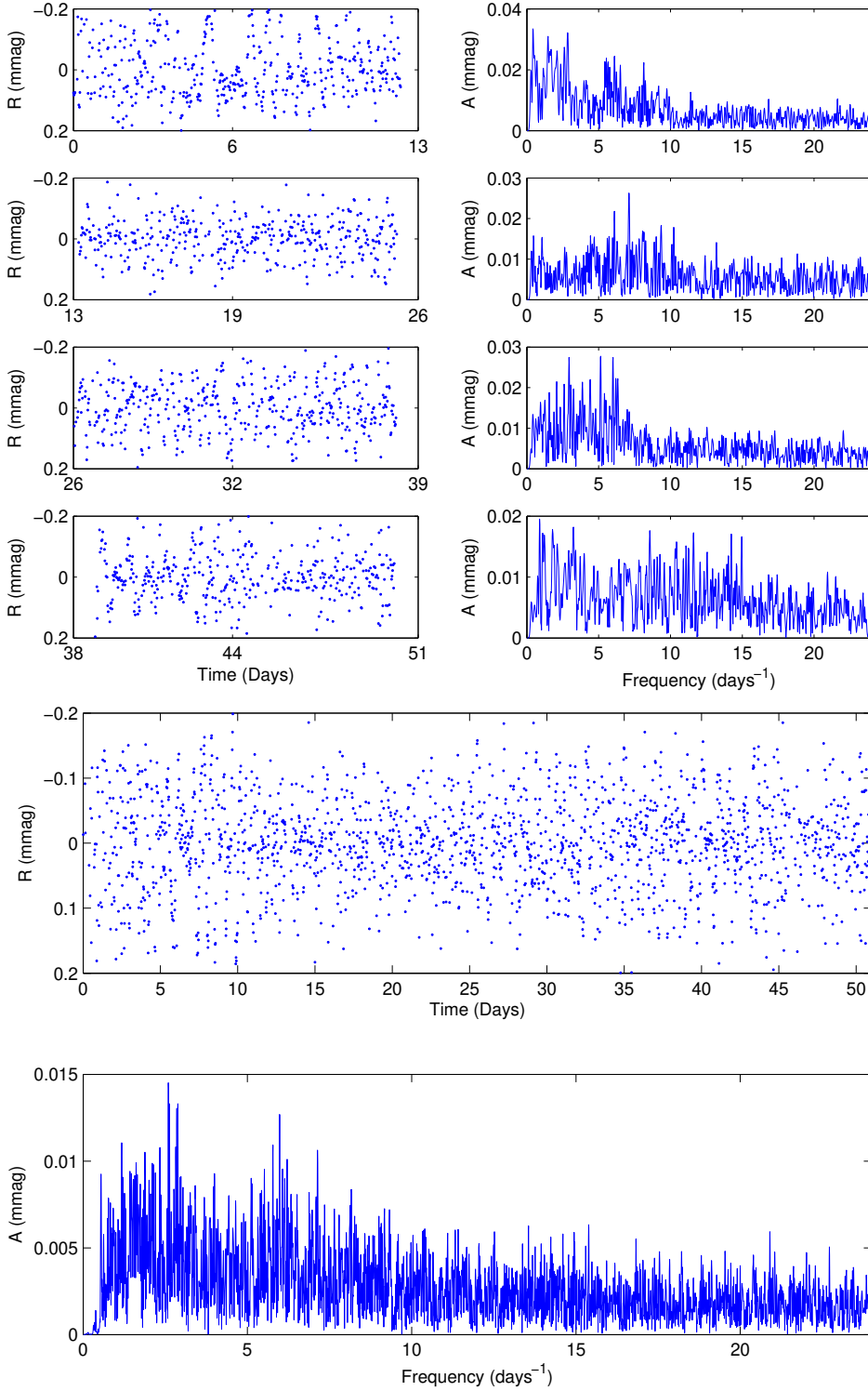


Figure C29. As Fig. 12, but for C18. Here the light curve was split into four segments. No evidence for pulsational signals is identified based on either method of analysis.